Nonlinear Infrared Polaritonic Interaction between Cavities Mediated by Molecular Vibrations at Ultrafast Timescale

Bo Xiang^{†2}, Jiaxi Wang^{†1}, Zimo Yang², Wei Xiong^{1,2*}

¹Department of Chemistry and Biochemistry, UC San Diego, La Jolla, CA, 92093

²Materials Science and Engineering Program, UC San Diego, La Jolla, CA, 92093

ORCID: Wei Xiong 0000-0002-7702-0187, Bo Xiang 0000-0002-9055-7931, Jiaxi Wang 0000-0001-7663-6978

Abstract Realizing nonlinear interactions between spatially separated particles can advance new science and technology, including remote catalysis of chemical reactions, ultrafast processing of information in IR photonic circuitry, and new platforms for quantum simulations with increased complexity. In this report, we achieved nonlinear interactions at ultrafast timescale between polaritons contained in spatially adjacent cavities in the mid-infrared (IR) regime, altering polaritons in one cavity by pumping polaritons in an adjacent one. This was done by hybridizing molecular vibrational modes with photon modes, a process that combines characteristics of both photon delocalization and molecular nonlinearity. Thus, the dual photon/molecule character of polaritons enables nonlinearity delocalized between two adjacent cavities – a new property that neither molecular nor cavity mode would possess alone.

Teaser: Strong coupling enables nonlinearity delocalized between cavities by combining the delocalization of photon and molecular anharmonicity – the best of both worlds.

Introduction

Nonlinear interactions between molecular vibrational modes, referred as molecular vibrational nonlinearity hereafter, are crucial to distribute energies among chemical groups during reactions. However, they are localized within angstroms due to the physical dimensions of molecular potential energy surfaces, e.g. Morse or double well potentials. Even intermolecular nonlinear interactions through dipole-dipole interactions are limited to a few nanometers. Because the molecular vibrational nonlinearity is localized, the reactants have to be close to each other in liquid phase to react, which makes many reactions limited by diffusions. Being able to delocalize nonlinear interactions across micron-length thus has the potential to trigger reactions without the reactants to be close in spaces. Meanwhile, nonlinear interactions of photons are the crucial components for photonic circuitry (1,2), and such interactions in the mid-IR regime can enable chemical sensing at molecular fingerprints region. However, scaling up of these developments are prohibited, because nonlinear IR photonic interactions are also localized, which are mediated by molecules. Thus, delocalized nonlinear interactions in the IR regime could be critical for future photonic applications.

In this work, we report nonlinearity between polaritons in two adjacent cavities. By exciting polaritons in one cavity, we affect polaritons in the neighboring cavity, whose geometric center is tens of micron away from the first cavity, through strong coupling between the vibrational and cavity modes (3-12). The strong coupling between molecular vibrational and cavity modes forms molecular vibrational polaritons, which enables novel phenomena such as vibrational energy transfer between molecules in the liquid phase (13), and modified chemical reaction selectivity (14). The local molecular vibrational anharmonicity provides sources of optical nonlinearity, while photon cavity modes are macroscopic and delocalized but linear. The strong light-matter coupling then combines photon delocalization with molecular nonlinearity, which otherwise would not exist in either mode alone. We note that the idea of combining material nonlinearity with hybridized cavities was first proposed in atomic-molecular-physics for quantum simulation (15), and

recently demonstrated in inorganic semiconductor exciton-polaritons (16, 17). To the best of our knowledge, this report is the first work to enable intercavity nonlinearity with liquid phase *molecular* systems, and to directly time-resolve the dynamics of the nonlinear interaction between polaritons in adjacent cavities. We refer to this nonlinearity as polaritonic intercavity nonlinear interactions.

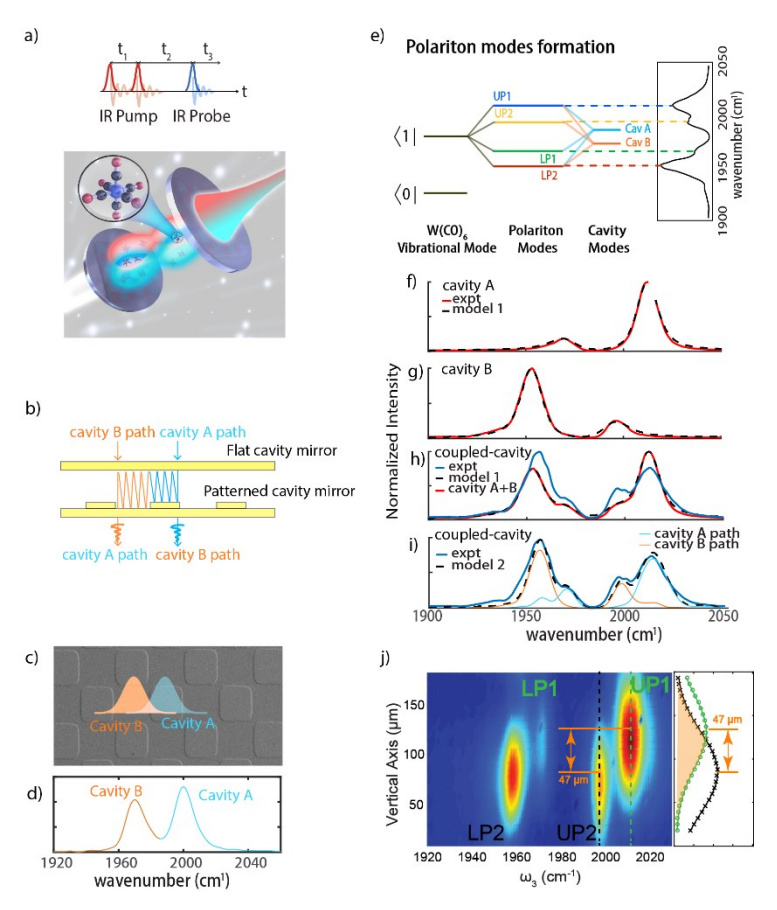


Figure 1. Key idea of intercavity nonlinear interactions between polaritons. (a) Illustration of a coupled-cavity and 2D IR pulse sequence. The key to enable intercavity nonlinear interaction is to have anharmonic molecules (enlarged) in the shared volume between cavities. (b) A proposed mechanism of coupling between cavities. When a photon enters into cavity A, it hops to cavity B and exits from there (cavity A path). The reversed direction (cavity B path) could happen too. (c) SEM of checkerboard-patterned cavity mirror. (d) FTIR of the dual cavity modes (1970 cm⁻¹ and 2000 cm⁻¹). (e) Energy diagram of polariton modes formed by the coupling of W(CO)₆ with the coupled-cavity. (f-i) Experimental and simulated linear IR of polaritons. (f and g) Polariton tranmission spectra in a regular cavity detuned to match the resonance of cavity A and B, which can be well fitted by model 1. (h) Experimental polariton tranmission spectra of the coupled cavity and the summbed spectra of panels f and g. (i) Experimental and simulated linear IR of polaritons in the coupled cavity. Using model 2 (see main text and S2.2 for details), the experimental spectra can be well simulated. Additional minor polariton peaks appear due to delocalization to the neighboring modes. (j) Transmission image of coupled -cavity polariton system where LP1/UP1 states (cavity A polaritons) locate at the top part while the LP2/UP2 states (cavity B polaritons) locate at bottom part. The spatial separation between cavity A and cavity B polaritons is 47 μm, close to the pattern size of 50 μm. There is a substantial overlapping area between the two modes as a result of mode delocalization, which is highlighted as an orange area on the right panel

Results

To realize polaritonic intercavity nonlinear interactions, we fabricate a coupled Fabry-Perot (FP) cavity and conduct linear and nonlinear IR spectroscopy on coupled-cavity polaritons. A checkerboard matrix is composed of individual FP cavities, where cavities with two thicknesses (12.50 µm and 12.69 µm for cavity

A and B respectively), and two distinct transition frequencies (1970 and 2000 cm⁻¹, Figure 1d), alternate (Figure 1b and c for SEM image, See SM Methods). Here, neighboring cavities can overlap through evanescent waves along the transverse directions (Figure 1j), and the molecular modes in the overlapping volumes should enable nonlinear interactions (4, 6, 7) between polaritons in adjacent cavities (Figure 1a). Experimentally, we found that the optimal cavity lateral dimension was 50 μm. We believe that at this size, it ensures a sufficient interaction between neighboring cavities while keeping the two cavity modes distinguishable. Furthermore, because the IR laser beam is about 100 μm, cavity with this size avoid inhomogeneity introduced by pumping too many cavities together. We prepared the polaritons by encapsulating a saturated W(CO)₆/hexane solution (~40 mM) in the coupled-cavity (see SM Methods (3, 6)). W(CO)₆ has a strong asymmetric stretch vibrational mode at 1983 cm⁻¹, which is ideal for forming polaritons in the IR regime.

The linear IR spectra of polaritons in the coupled-cavity show four spectral peaks (the right part of Figure 1e), which is surprising and makes the transfer matrix model (18) challenging to capture the results. From a naïve perspective, if one molecular vibrational mode strongly couples to the two-cavity modes simultaneously, three IR peaks would be expected (see SM S3.4 for details), which disagrees with the observed four-peak feature. An alternative model is that the molecular vibrations couple to the two cavities separately, each forming one pair of polaritons (upper polariton, UP, and lower polariton, LP), i.e., UP1 and LP1 in cavity A and UP2 and LP2 in cavity B, respectively, composing the total four peaks. To test this idea, we measure the IR spectra of two polariton systems prepared by regular FP cavities, e.g., UP1/LP1 and UP2/LP2, separately (Figure 1f and g), and then add them together numerically. The peak positions of the summed spectrum match well with the experimental spectrum, but the intensities do not (Figure 1h). Similarly, while the transfer matrix method (18) (model 1, see SM S2.1) can simulate polariton spectra of each cavity perfectly (dashed line in Figure 1f and g), it cannot reproduce the spectral intensity of the polaritons in the coupled cavity (dashed line in Figure 1h).

The intensity mismatch suggests a component is missing from the transfer matrix model to account for the intensity redistribution among spectral peaks. We extended the transfer matrix model by including photon hopping (model 2) and show that the missing component is the delocalization of cavity modes: Upon entering cavity A, photons can hop to cavity B and subsequently interact with molecular vibrations in cavity B, representing the delocalization between cavities (referred to as the cavity A path in Figure 1b). An alternative path also exists (cavity B path in Figure 1b). The expression of transmission spectra based on model 2 is summarized in Eq.1 (detailed derivation in S2.2).

$$T = \left[\frac{T_1 e^{-\frac{1}{2}\alpha L_1}}{1 - R_1 e^{i\Delta\varphi_1 - \alpha L_1}} \left(1 - R_1^n e^{-n\alpha L_1 + in\Delta\varphi_1} \right) + \frac{\sqrt{T_1 T_2} e^{-\frac{1}{2}\alpha L_1}}{1 - R_2 e^{i\Delta\varphi_2 - \alpha L_2}} \left(R_1^{n-1} e^{-(n-1)\alpha L_1 + i(n-1)\Delta\varphi_1} R_2 e^{-\alpha L_2 + i\Delta\varphi_2} \right) \right]^2$$
For 1

where T_m , R_m , L_m and $\Delta \varphi_m$ are transmission, reflection, cavity thickness, and phase shift of cavity m, respectively, α is the absorptive coefficient of molecules, and n represents the number of round trips before photon hopping to the adjacent cavity. Results from model 2 reproduced not only the spectral peak position but also the intensities from the experimental measurements (Figure 1i, detailed model in SM S2.3 and fitting parameters in SM S3.2). The new model result shows that the linear IR spectra are a combination of two sets of polaritons from the cavity A and B paths, respectively (orange and cyan traces in Figure 1i). Thus, molecular modes in each cavity strongly couple to the cavity mode that they reside in and weakly couple to the adjacent cavity mode (Figure 1e). We note the intermolecular interaction are negligible to contribute to the change of linear IR (see SM S3.4 for details).

This theoretical picture is further supported by an IR hyperspectral image of the coupled-cavity polaritons. In this image (Figure 1j, detailed description of the IR hyperspectral imaging system in Fig.S9 in SM S3.8), a vertical slice of the coupled-cavity image is spectral dispersed horizontally and imaged by an FPA MCT detector. Thus, the vertical axis of the image represents the location of the polaritons and the horizontal axis corresponds to the frequency of the polariton features. We can identify the UP1 and LP1 from cavity A at 116 μ m, and UP2 and LP2 from cavity B at 69 μ m. All polaritons reside at their characteristic frequency on the horizontal axis, and they are spatially displaced along the vertical by 47 μ m, agreeing with the SEM image. However, vertical cuts show polaritons in each cavity leak into their neighboring cavity, as the width

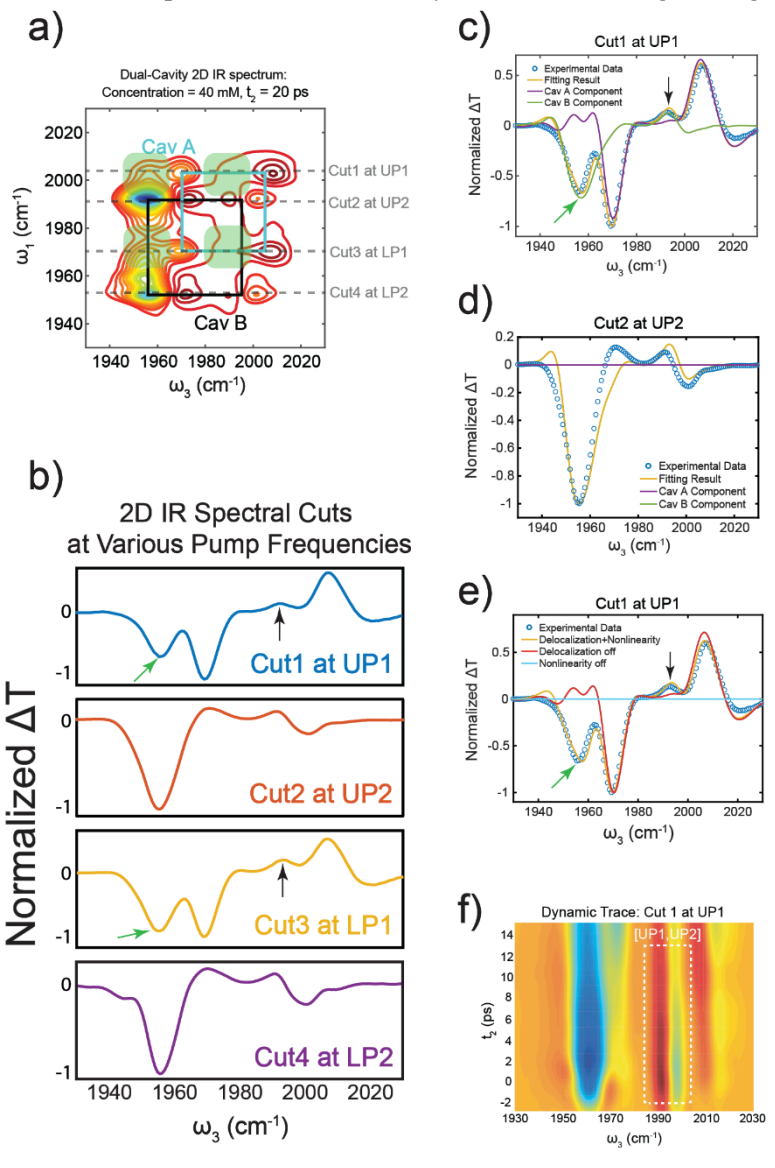


Figure 2. 2D IR spectra to show intercavity nonlinear interactions between polaritons. a) 2D IR of $W(CO)_6$ /hexane in coupled dual cavity. Cross peaks between polaritons from different cavities are observed (in shaded green area). The 2D IR peaks that are solely from cavity A are at the corner of blue square and that of cavity B are at the corners of black square. The spectrum was taken with the incident IR beam to be 11.3 degreee. b) Pump spectral cuts of 2D IR in a) at $\omega_{pump} = \omega_{UP1}$ (blue), ω_{UP2} (red), ω_{LP1} (yellow), and ω_{LP2} (purple) also show cross peak features. The green and black arrows in b-e highlight the cross peaks due to intercavity nonlinear interactions. c) and d) Experimental (blue dots) and simulated (yellow) spectral cut at $\omega_{pump} = \omega_{UP1}$, and at $\omega_{pump} = \omega_{UP2}$, and the corresponding simulated contributions from cavity A (purple) and B (green) e) Experimental (blue dots) spectral cut at $\omega_{pump} = \omega_{UP1}$ and simulated cut spectrum with nonlinearity off (sky blue), with delocalization off (red), and delocalization and molecular nonlinearity together (yellow). (f) 2D IR dynamics at $\omega_{pump} = \omega_{UP1}$.

of polaritons are 59 and 64 μ m, larger than the 50 μ m dimension of the cavity. Therefore, the IR hyperspectral image also agree with the theoretical picture that cavity mode delocalization exists, which is a critical component for polaritonic intercavity nonlinear interactions (15). However, we have not yet demonstrated that polaritonic intercavity nonlinear interactions, in which excited polaritons influence those in an adjacent cavity, occurred.

To examine polaritonic intercavity nonlinear interactions, we conduct 2D IR spectroscopy (6, 9, 19–23). 2D IR measures the third-order nonlinear response of the systems. The pulse sequence described in Figure 1a excites two vibrational coherences at various time incidences and tracks the interaction and dynamics of quantum states (see SM Methods). For example, when two modes interact with each other, e.g., exciting one mode can affect the other mode, cross-peaks appear at the corner defined by the resonance frequencies of the two coupled modes.

2D IR spectra of the coupled-cavity polaritons show clear cross-peaks ($t_2 = 20$ ps, shown in shaded green areas in Figure 2a). In the following, we perform detailed spectral analysis to show these cross-peaks are signatures of polaritonic intercavity nonlinear interactions. Based on knowledge from previous publications (4–7, 19), we focus on analyzing 2D IR signal at t_2 that is longer than polariton lifetime, e.g., $t_2 = 20$ ps, where the physics is well understood: the source of nonlinear signals at is a non-equilibrium population of dark states of the W(CO)₆ asymmetric modes in the cavities. At the long-time limit, polaritons decay and excite dark modes, leading to the derivative signals near UP due to Rabi splitting contraction, and overtone absorptions for the strong absorptive feature at the LP side (detailed explanation in SM S3.1) (4, 6, 7).

To quantitively understand the spectra, we take cuts of the 2D spectra at several ω_{pump} , corresponding to pump-probe spectra by exciting specific polariton states, and simulate them using model 2 where α , the absorptive coefficient of molecules, will be changed by the the pump-induced ground-state molecular population reduction in both cavity components (details of simulation see Methods and S2.3). The simulated spectra match with the experimental results very well, capturing the derivative features on the UP side and the double absorptive features on the LP side (Figure 2c is a spectral cut at $\omega_{pump} = \omega_{UP1} = 2010$ cm⁻¹; simulations of other spectral cuts are in S3.2). The only mismatch is a small positive feature near 1940 cm⁻¹ due to lineshape changes appears in the simulated result but not the experimental data. This feature could be canceled in the experiment by higher order excited state absorptions of the reservoir mode – a term that was not included in the simulation.

Further physical insights of the intercavity nonlinear signal are obtained by decomposing the simulated spectra into contributions from cavities A and B. A representative result shows that both the cross-peaks of the spectral cut at UP1 of cavity A – a noticeable derivative feature near ω_{probe} =1995 cm⁻¹ and a large absorptive peak at ω_{probe} =1955 cm⁻¹ are derived from the nonlinear responses from cavity B (the green trace in Figure 2c). In contrast, the nonlinear signal of cavity A shows a tiny peak at ω_{probe} =1995 cm⁻¹ (the purple trace in Figure 2c). Because this spectral cut is obtained by pumping UP1 of cavity A, it confirms that exciting cavity A can affect polaritons in cavity B – a nonlinear interaction *delocalized* between cavities (similar results are shown when pumping LP1 in Fig. S4a).

Because the simulation shows that it is necessary to change the reservoir ground and excited state population in both cavities in order to reproduce the experimental results (dc1, dc12, dc2, and dc22 determine A_i (oscillator strength of the ground and excited dark reservoir states) in equation S18 in SM S2.3, and see table S1 in SM S3.2 for the values to simulate the experimental data), it suggests that the changes of reservoir population lead to the observed nonlinear signals. Thus, the source of polaritonic intercavity nonlinear interaction is polariton-reservoir mode interactions (similar to those observed in exciton polaritons(24)), in which excited polaritons in cavity A transfer their population to dark reservoir modes, a

portion of which is shared with cavity B. The shared excited dark modes reduced the Rabi splitting of polaritons in cavity B and introduce absorptions of the excited dark modes, thereby generating nonlinear signals.

We note that such a nonlinear interaction is not detected in spectral cuts of exciting UP2 (Fig.2d) or LP2 (Fig. S4b) of cavity B, as the cavity B contribution can well simulate these spectral cuts. Further study on the 2D IR spectra suggest that the intercavity interaction cross peaks are highly sensitive to the incident angle (SM S3.7): at certain angle the interactions are mutual between two cavities, i.e. cross peaks exist when either cavity is excited; whereas at other angles, interactions are optimized in one direction, i.e. only cross peaks due to exciting either cavity A or B exist. The angular sensitivity further demonstrates that the intercavity polariton-interaction are originated from photon hopping which highly depends on beam angles, instead of intermolecular interactions. The physical origin of this dependence is beyond our modified transfer matrix model (eq.1), which warrants momentum imaging experiments and more comprehensive theoretical studies in the future. Without further notification, all 2D IR study are done at angle = 11.3°, where the cavity A to B interactions are favorable.

Both cavity delocalization and molecular nonlinearity are critical for polaritonic intercavity nonlinear interactions, as shown by turning off either factor (Figure 2e). When delocalization is turned off, a simulated spectrum is similar to the ones of single cavity polaritons (the red trace in Figure 2e). When molecular nonlinearity is turned off by setting anharmonicity to zero, there are simply no signals (the light-blue trace in Figure 2e).

The crucial roles of cavity delocalization and molecular nonlinearity can be viewed from the theoretical aspect. In the polariton system, the nonlinear interactions are a result of molecular anharmonicity, which can be written as

$$H_{int} = Va^{+}a^{+}aa = V\sum_{k_{1},k_{2},k_{3},k_{4}}^{UP1,UP2,LP1,LP2}c_{k_{1}}^{*}c_{k_{2}}^{*}c_{k_{3}}c_{k_{4}}a_{k_{1}}^{+}a_{k_{2}}^{+}a_{k_{3}}a_{k_{4}}$$
 Eq.2

H_{int} is the interaction term of the full polariton Hamiltonian (4), Where a^+ and a are the creation and annihilation operators of the molecular vibrational modes in a cavity, and the interaction is local. To derive the second part of the equation, we rewrite $a^+ = c_{UP1}^* a_{UP1}^+ + c_{LP1}^* a_{LP1}^+ + c_{UP2}^* a_{UP2}^+ + c_{LP2}^* a_{LP2}^+$, where c can be derived from Hopfield coefficient. Terms like $|c_{LP1}|^2 |c_{UP2}|^2 a_{LP1}^+ a_{LP1}^+ a_{UP2}^+ a_{UP2}^+$ exist in the second part of Eq.2, which leads to the nonlinear interaction between LP1 and UP2. The strength of this intercavity polaritonic interaction depends on the coefficient $|c_{LP1}|^2 |c_{UP2}|^2$, and therefore delocalization. For example, if the molecular modes are localized in cavity A, which makes $c_{UP2} = 0$, such an interaction disappears. It is the strong light-matter coupling and photon hopping that render the local molecular mode a linear combination of polaritons in different cavities, and thereby delocalize the nonlinearity.

The role of mixing Hopfield coefficient is verified by manipulating the polaritonic intercavity nonlinear interactions through changing molecular concentration, and thereby Rabi splitting. No apparent 2D IR signature of intercavity coupling appears for the polariton at lower concentrations (26 mM, Fig. 3a). Spectral cuts at $\omega_1 = \omega_{UP1}$, and ω_{LP1} further confirm this observation (Fig. 3b, more details are shown in SM, S3.3). This result also serves as a control experiment to show that the observed cross-peaks are not photonic artifacts (e.g., spectral filter effects). We further extract the relative population of excited dark modes in cavity B, when polaritons in A are excited from the 2D IR results, at various Rabi splitting (SM S3.3). The relative population decreases from 24.0% to 3.5%, as the molecular concentration declines from 40 mM to 26 mM (Fig.3d). These results qualitatively agree with the result from the four-by-four Hamiltonian matrix model that describe the coupled-cavity polaritons (SM S3.4). Lowering the concentration results in fewer shared vibrational modes between the two cavities. As summarized in Fig 3c, large Rabi-spliting leads to that a non-negligible amount of vibrational modes in cavity B (vib-B)

participates in the formation of LP1 and UP1 states, and a portion of vib-A composes LP2 and UP2. Upon pumping LP1 and UP1, it excites the shared vib-A and -B populations, perturbing the energy levels of LP2 and UP2. With small concentration, such a state-mixing between cavities becomes negligible, causing polaritonic intercavity nonlinear interaction to disappear.

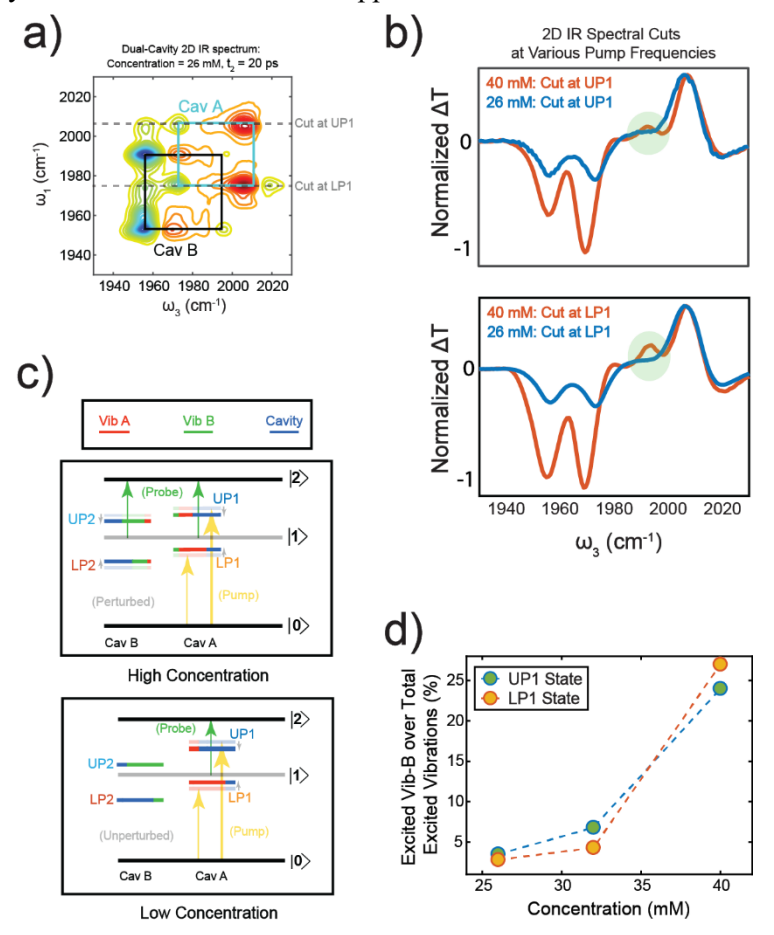


Figure 3. 2D IR spectrum of dual cavity-polaritons at small Rabi splitting. a) 2D IR of $W(CO)_6$ /hexane in coupled dual cavity with 26 mM molecular concentration; The 2D IR peaks that are solely from cavity A are at the corner of blue square and that of cavity B are at the corners of black square. b) Pump spectral cuts of 2D IR at $\omega_{pump} = \omega_{UP1}$ and ω_{LP1} (blue/red traces for polariton system with 26/40 mM molecular concentration, both are at $t_2 = 20$ ps) confirm the absence of clear cross peaks with smaller molecular concentration. All data were collected with the incidence IR beam to be 11.3 deg. c) Schematic illustration of the intercavity coupling enabled/disabled in dual cavity systems with high/low molecular concentration (top/bottom panel), $|0\rangle$, $|1\rangle$, $|2\rangle$ are the ground, first excited and second excited states of the reservoir modes; gray levels indicates the modes are optically dark d) Percentage of excited Vib-B among the total excited vibrational modes in cavity A as a function of molecular concentration, extracted from the spectral fitting results.

We lastly measure the dynamics of the cross-peaks (Fig. 2f), by scanning the waiting time t_2 of the 2D IR spectra. The spectral cut dynamic around $\omega_1 = \omega_{UP1} = 1995$ cm⁻¹ (Fig. 2f, 2D IR cut at UP1 in the dashed white box) shows $[\omega_{UP1}, \omega_{UP2}]$ cross-peak appears within the polariton lifetime (< 3 ps, a similar trend can be observed when cutting at $\omega_1 = \omega_{LP1}$ as well, see SM S3.6). This result agrees with the mechanism that the evanescent wave of cavity mode leads to the polaritonic intercavity nonlinear interactions, because the photon hopping can only happen before it leaks out of the cavity.

Discussion

The photonic intercavity nonlinear interaction is exclusively a result of the joint merits of the evanescent wave of cavity modes and molecular nonlinearity. By combining them, a unique new property is created which does not exist in either mode. This demonstration could enable polaritonic photonic circuitry in the molecular fingerprint IR regime for low-concentration threshold, compact chemical sensing. The micronrange nonlinear interaction can be further extended to even longer distances when combined with polariton propagation. This experiment also lays a foundation for remote chemistry (25), enabling chemistry in one cavity by manipulation of molecules (e.g., as catalysts) in the other cavity. By selectively pumping using a pulse shaper (26), the coupled cavity can be a new platform for entangled polaritonic qubits.

METHODS.

Fabrication of couple-cavity optical mirror. In order to generate two cavity modes with specific frequency, two different path lengths need to be achieved within one pair of cavity mirrors. A checkerboard pattern is designed and fabricated on the CaF₂ window using photolithography, followed by sputtering deposition of a layer of ZnO and lift-off of ZnO deposited on photoresist, thus leaving behind a checkerboard patterned layer of ZnO on CaF₂. Dielectric coatings (Thin Film Corp.) are deposited on both the flat CaF₂ window and the CaF₂ window with patterned ZnO layer to obtain ~96% reflectivity at around 5 μ m wavelength. In this work, a dielectric-coated flat CaF₂ and a dielectric-coated CaF₂ with patterned ZnO (~200-nm thickness) are used in tandem to generate dual cavity modes separated by ~30 cm⁻¹ at 5 μ m. The frequency separation between the two cavity modes can be tuned by controlling the thickness of the ZnO layer.

Sample Preparation. The W(CO)₆ (Sigma-Aldrich)/coupled-cavity system is prepared in an IR spectral cell (Harrick) containing one flat dielectric CaF₂ mirror and one checkerboard-patterned dielectric CaF₂ mirror, separated by a 12.5 μm Teflon spacer and filled with W(CO)₆/hexane solution with various concentrations (40 Mm, saturated concentration, 32 mM and 26 mM). The regular W(CO)₆/cavity system is prepared in the same way in an IR spectral cell with two flat dielectric CaF₂ mirrors. The cavity mode finesse is around 14 with $\lambda_{FSR}/\Delta\lambda c$, where λ_{FSR} is the free spectral range and $\Delta\lambda c$ is the FWHM of the resonance.

2D IR spectroscopy. Two-dimensional infrared (2D IR) spectroscopy (21) is applied to investigate the light-matter interaction of a W(CO)₆/microcavity system (detailed 2D IR set up, and data acquisition is described in S1.2). Briefly, a pump-probe geometry is adopted where three IR pulses (Fig. 1a) interact with sample systems. The first IR pump pulse and probe pulse generate two coherent states in the system in t_1 and t_3 , respectively, which will later be Fourier transformed to the frequency domain as ω_1 (pump frequency) and ω_3 (probe frequency). The second IR pump pulse puts the system in a population state during t_2 . All 2D IR spectra in this work are taken at $t_2 = 20$ ps to avoid interference between pump and probe pulses.

References

- 1. O. Wada, Femtosecond all-optical devices for ultrafast communication and signal processing. *New J. Phys.* **6** (2004), pp. 1–35.
- 2. D. Ballarini, M. De Giorgi, E. Cancellieri, R. Houdré, E. Giacobino, R. Cingolani, A. Bramati, G. Gigli, D. Sanvitto, All-optical polariton transistor. *Nat. Commun.* **4**, 1778 (2013).
- 3. B. S. Simpkins, K. P. Fears, W. J. Dressick, B. T. Spann, A. D. Dunkelberger, J. C. Owrutsky, Spanning Strong to Weak Normal Mode Coupling between Vibrational and Fabry-Pérot Cavity Modes through Tuning of Vibrational Absorption Strength. *ACS Photonics*. **2**, 1460–1467 (2015).
- 4. R. F. Ribeiro, A. D. Dunkelberger, B. Xiang, W. Xiong, B. S. Simpkins, J. C. Owrutsky, J. Yuen-Zhou, Theory for Nonlinear Spectroscopy of Vibrational Polaritons. *J. Phys. Chem. Lett.* **9**, 3766–3771 (2018).
- 5. A. D. Dunkelberger, R. B. Davidson, W. Ahn, B. S. Simpkins, J. C. Owrutsky, Ultrafast Transmission Modulation and Recovery via Vibrational Strong Coupling. *J. Phys. Chem. A.* **122**, 965–971 (2018).
- 6. B. Xiang, R. F. Ribeiro, A. D. Dunkelberger, J. Wang, Y. Li, B. S. Simpkins, J. C. Owrutsky, J. Yuen-Zhou, W. Xiong, Two-dimensional infrared spectroscopy of vibrational polaritons. *Proc. Natl. Acad. Sci. U. S. A.* **115**, 4845–4850 (2018).
- 7. A. D. Dunkelberger, B. T. Spann, K. P. Fears, B. S. Simpkins, J. C. Owrutsky, Modified relaxation dynamics and coherent energy exchange in coupled vibration-cavity polaritons. *Nat. Commun.* 7, 13504 (2016).
- 8. X. Liu, T. Galfsky, Z. Sun, F. Xia, E. C. Lin, Y. H. Lee, S. Kéna-Cohen, V. M. Menon, Strong light-matter coupling in two-dimensional atomic crystals. *Nat. Photonics.* **9**, 30–34 (2014).
- 9. B. Xiang, R. F. Ribeiro, Y. Li, A. D. Dunkelberger, B. B. Simpkins, J. Yuen-Zhou, W. Xiong, Manipulating Optical Nonlinearities of Molecular Polaritons by Delocalization. *Sci. Adv.* 5, eaax5196 (2019).
- 10. K. E. Dorfman, S. Mukamel, Multidimensional photon correlation spectroscopy of cavity polaritons. *Proc. Natl. Acad. Sci. U. S. A.* **115**, 1451–1456 (2018).
- 11. M. Stührenberg, B. Munkhbat, D. G. Baranov, J. Cuadra, A. B. Yankovich, T. J. Antosiewicz, E. Olsson, T. Shegai, Strong Light-Matter Coupling between Plasmons in Individual Gold Bipyramids and Excitons in Mono- and Multilayer WSe2. *Nano Lett.* **18**, 5938–5945 (2018).
- 12. T. E. Li, H.-T. Chen, A. Nitzan, J. E. Subotnik, Quasiclassical modeling of cavity quantum electrodynamics. *Phys. Rev. A.* **101**, 033831 (2020).
- 13. B. Xiang, R. F. Ribeiro, M. Du, L. Chen, Z. Yang, J. Wang, J. Yuen-Zhou, W. Xiong, Intermolecular vibrational energy transfer enabled by microcavity strong light–matter coupling. *Science* (80-.). **368** (2020), pp. 665–667.
- 14. A. Thomas, L. Lethuillier-Karl, K. Nagarajan, R. M. A. Vergauwe, J. George, T. Chervy, A. Shalabney, E. Devaux, C. Genet, J. Moran, T. W. Ebbesen, Tilting a ground-state reactivity landscape by vibrational strong coupling. *Science* (80-.). 363, 615–619 (2019).
- 15. M. J. Hartmann, F. G. S. L. Brando, M. B. Plenio, Strongly interacting polaritons in coupled arrays of cavities. *Nat. Phys.* **2**, 849–855 (2006).

- 16. S. R. K. Rodriguez, A. Amo, I. Sagnes, L. Le Gratiet, E. Galopin, A. Lemaître, J. Bloch, Interaction-induced hopping phase in driven-dissipative coupled photonic microcavities. *Nat. Commun.* 7, 11887 (2016).
- 17. S. Kim, Y. G. Rubo, T. C. H. Liew, S. Brodbeck, C. Schneider, S. Höfling, H. Deng, Emergence of microfrequency comb via limit cycles in dissipatively coupled condensates. *Phys. Rev. B.* **101**, 085302 (2020).
- 18. G. Khitrova, H. M. Gibbs, F. Jahnke, M. Kira, S. W. Koch, Nonlinear optics of normal-mode-coupling semiconductor microcavities. *Rev. Mod. Phys.* **71**, 1591–1639 (1999).
- 19. B. Xiang, R. F. Ribeiro, L. Chen, J. Wang, M. Du, J. Yuen-Zhou, W. Xiong, State-Selective Polariton to Dark State Relaxation Dynamics. *J. Phys. Chem. A.* **123**, 5918–5927 (2019).
- 20. P. Saurabh, S. Mukamel, Two-dimensional infrared spectroscopy of vibrational polaritons of molecules in an optical cavity. *J. Chem. Phys.* **144**, 124115 (2016).
- 21. P. Hamm, M. Zanni, *Concepts and methods of 2D infrared spectroscopy* (Cambridge University Press, Cambridge, 2011), vol. 9781107000.
- 22. J. A. Fournier, W. B. Carpenter, N. H. C. Lewis, A. Tokmakoff, Broadband 2D IR spectroscopy reveals dominant asymmetric H5O2+ proton hydration structures in acid solutions. *Nat. Chem.* **10**, 932–937 (2018).
- 23. D. V. Kurochkin, S. R. G. Naraharisetty, I. V. Rubtsov, A relaxation-assisted 2D IR spectroscopy method. *Proc. Natl. Acad. Sci. U. S. A.* **104**, 14209–14214 (2007).
- 24. T. Yagafarov, D. Sannikov, A. Zasedatelev, K. Georgiou, A. Baranikov, O. Kyriienko, I. Shelykh, L. Gai, Z. Shen, D. Lidzey, P. Lagoudakis, Mechanisms of blueshifts in organic polariton condensates. *Commun. Phys.* **3**, 18 (2020).
- 25. M. Du, R. F. Ribeiro, J. Yuen-Zhou, Remote Control of Chemistry in Optical Cavities. *Chem.* 5, 1167–1181 (2019).
- 26. Z. Yang, B. Xiang, W. Xiong, Controlling Quantum Pathways in Molecular Vibrational Polaritons. *ACS Photonics*. **7**, 919–924 (2020).

Acknowledgments: We thank Dr. Yuen-Zhou and Dr. Raphael F. Ribeiro's constructive feedback to this work. Funding: This work is supported by NSF CAREER Award DMR1848215. The fabrication of dual-cavity mirrors was performed in part at the San Diego Nanotechnology Infrastructure (SDNI) of UCSD, a member of the National Nanotechnology Coordinated Infrastructure, which is supported by the National Science Foundation (Grant ECCS-1542148). B.X. is supported by a Roger Tsien Fellowship from the Department of Chemistry and Biochemistry at UC San Diego. Author Contributions: W.X. conceived the original idea and developed the theoretical model for linear and nonlinear spectroscopy in this work. J.W. design and fabricated the coupled-cavity mirrors. J.W. and B.X. conducted 2D IR experiments, analyzed the data, and performed simulations. Z.Y. contributed to data analysis. J.W., B.X., and W.X. wrote the manuscript. Competing interests: Authors declare no competing interests. Data and materials availability: All data is available in the main text or the supplementary materials.

Author Information.

Affiliations

Department of Chemistry and Biochemistry, University of California, San Diego, La Jolla, CA, 92093 Jiaxi Wang, Wei Xiong

Materials Science and Engineering Program, University of California, San Diego, La Jolla, CA,92093 Bo Xiang, Zimo Yang, Wei Xiong

Corresponding author

*Correspondence to Wei Xiong.

Supplementary Materials:

Experimental Methods

Theory for Intercavity Polariton-Polariton Interaction

Supplementary Data

Figures S1 to S10

Tables S1 to S4

Figures and Tables

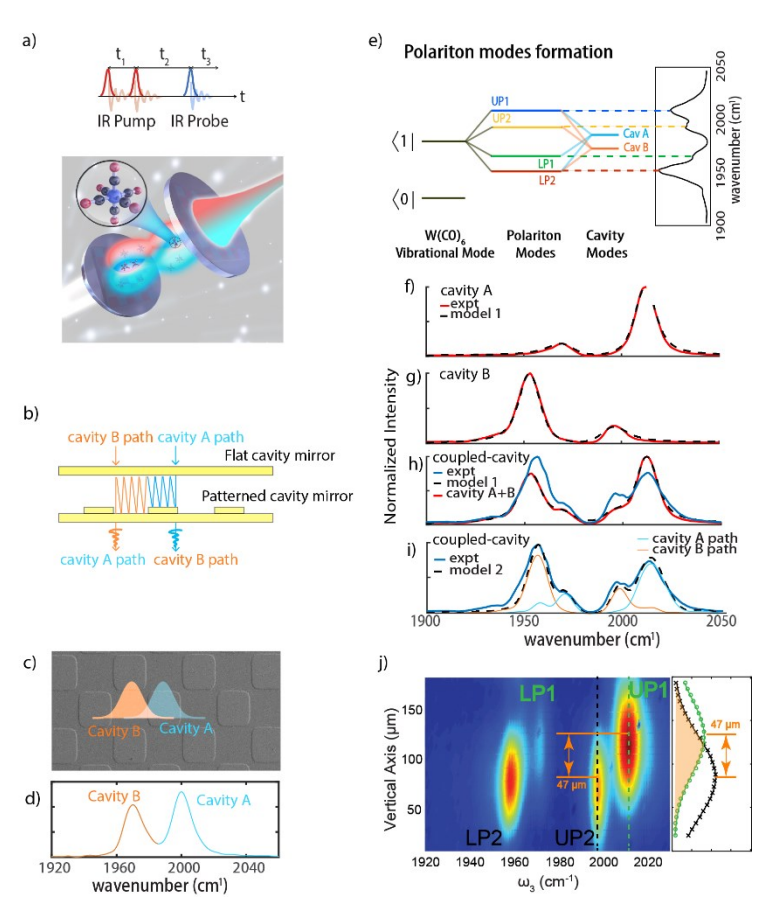


Figure 3. Key idea of intercavity nonlinear interactions between polaritons. (a) Illustration of a coupled-cavity and 2D IR pulse sequence. The key to enable intercavity nonlinear interaction is to have anharmonic molecules (enlarged) in the shared volume between cavities. (b) A proposed mechanism of coupling between cavities. When a photon enters into cavity A, it hops to cavity B and exits from there (cavity A path). The reversed direction (cavity B path) could happen too. (c) SEM of checkerboard-patterned cavity mirror. (d) FTIR of the dual cavity modes (1970 cm⁻¹ and 2000 cm⁻¹). (e) Energy diagram of polariton modes formed by the coupling of W(CO)₆ with the coupled-cavity. (f-i) Experimental and simulated linear IR of polaritons. (f and g) Polariton tranmission spectra in a regular cavity detuned to match the resonance of cavity A and B, which can be well fitted by model 1. (h) Experimental polariton tranmission spectra of the coupled cavity and the summbed spectra of panels f and g. (i) Experimental and simulated linear IR of polaritons in the coupled cavity. Using model 2 (see main text and S2.2 for details), the experimental spectra can be well simulated. Additional minor polariton peaks appear due to delocalization to the neighboring modes. (j) Transmission image of coupled -cavity polariton system where LP1/UP1 states (cavity A polaritons) locate at the top part while the LP2/UP2 states (cavity B polaritons) locate at bottom part. The spatial separation between cavity A and cavity B polaritons is 47 μm, close to the pattern size of 50 μm. There is a substantial overlapping area between the two modes as a result of mode delocalization, which is highlighted as an orange area on the right panel

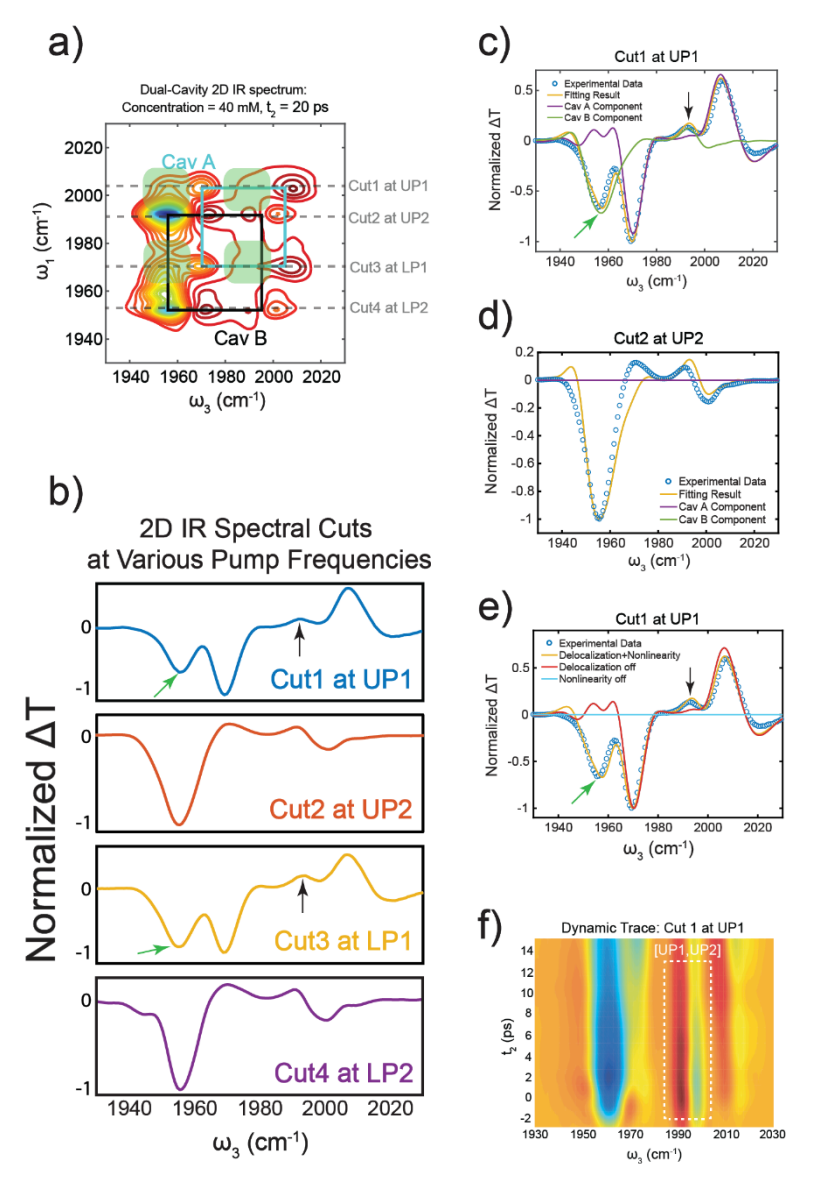


Figure 4. 2D IR spectra to show intercavity nonlinear interactions between polaritons. a) 2D IR of $W(CO)_6$ /hexane in coupled dual cavity. Cross peaks between polaritons from different cavities are observed (in shaded green area). The 2D IR peaks that are solely from cavity A are at the corner of blue square and that of cavity B are at the corners of black square. The spectrum was taken with the incident IR beam to be 11.3 degreee. b) Pump spectral cuts of 2D IR in a) at $ω_{pump} = ω_{UP1}$ (blue), $ω_{UP2}$ (red), $ω_{LP1}$ (yellow), and $ω_{LP2}$ (purple) also show cross peak features. The green and black arrows in b-e highlight the cross peaks due to intercavity nonlinear interactions. c) and d) Experimental (blue dots) and simulated (yellow) spectral cut at $ω_{pump} = ω_{UP1}$, and at $ω_{pump} = ω_{UP1}$, and at $ω_{pump} = ω_{UP1}$ and simulated contributions from cavity A (purple) and B (green) e) Experimental (blue dots) spectral cut at $ω_{pump} = ω_{UP1}$ and simulated cut spectrum with nonlinearity off (sky blue), with delocalization off (red), and delocalization and molecular nonlinearity together (yellow). (f) 2D IR dynamics at $ω_{pump} = ω_{UP1}$.

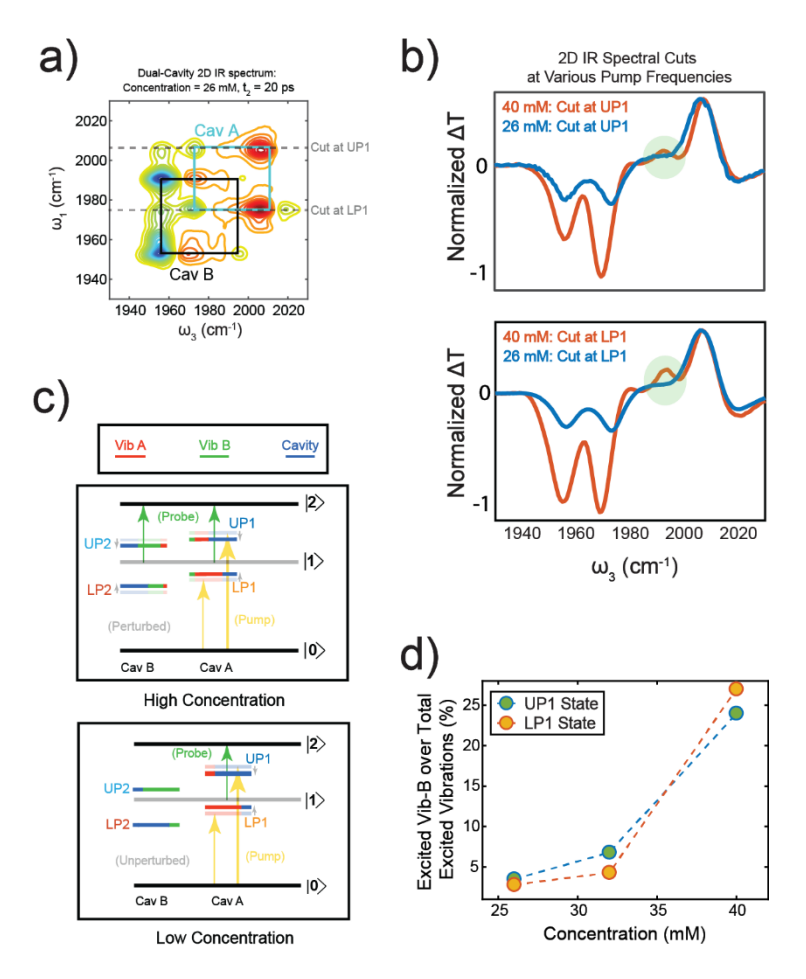


Figure 3. 2D IR spectrum of dual cavity-polaritons at small Rabi splitting. a) 2D IR of $W(CO)_6$ /hexane in coupled dual cavity with 26 mM molecular concentration; The 2D IR peaks that are solely from cavity A are at the corner of blue square and that of cavity B are at the corners of black square. b) Pump spectral cuts of 2D IR at $\omega_{pump} = \omega_{UP1}$ and ω_{LP1} (blue/red traces for polariton system with 26/40 mM molecular concentration, both are at $t_2 = 20$ ps) confirm the absence of clear cross peaks with smaller molecular concentration. All data were collected with the incidence IR beam to be 11.3 deg. c) Schematic illustration of the intercavity coupling enabled/disabled in dual cavity systems with high/low molecular concentration (top/bottom panel), $|0\rangle$, $|1\rangle$, $|2\rangle$ are the ground, first excited and second excited states of the reservoir modes; gray levels indicates the modes are optically dark d) Percentage of excited Vib-B among the total excited vibrational modes in cavity A as a function of molecular concentration, extracted from the spectral fitting results.

Supplementary Materials

- S1 Experimental Methods
- **S1.1 Materials and Methods**
- S1.2 2D IR Spectroscopy of W(CO)₆ Coupled to Dual Cavity Modes.
- S2 Theory for Intercavity Polariton-Polariton Interaction
- S2.1 Model for Transmission of a Single Fabry-Pérot Cavity Model 1
- S2.2 Model for the Transmission of Dual Cavity Model 2
- S2.3 Pump-Probe Fitting Model Based on Model 2
- S3 Supplementary Data
- S3.1 Transient Pump-Probe and 2D IR Spectra of Molecular Vibrational Polariton Systems
- S3.2 Simulation of Spectral Cuts of 2D IR of 40-mM W(CO)₆ in Hexane
- S3.3 2D IR Spectral Features of Polariton Systems with Various Concentrations
- S3.4 Four-by-Four Matrix Models the Intercavity Coupling along with Coupling between Cavity Modes and Molecular Vibrational Modes
- S3.5 Schematic Illustration of Photon Hopping Pathways
- S3.6 2D IR Dynamics
- S3.7 IR Incidence Angle Dependence
- S3.8 Transmission IR Image of Coupled-Cavity Polaritons
- S3.9 2D IR Spectrum of Combination of Detuned Regular Systems

S1 Experimental Methods

S1.1 Materials and Methods.

Fabrication of couple-cavity optical mirror

In order to generate two cavity modes with specific frequency, two different path lengths need to be achieved within one pair of cavity mirrors. A checkerboard pattern is designed and fabricated on the CaF_2 window using photolithography, followed by sputtering deposition of a layer of ZnO and lift-off of ZnO deposited on photoresist, thus leaving behind a checkerboard patterned layer of ZnO on CaF_2 . Dielectric coatings (Thin Film Corp.) are deposited on both the flat CaF_2 window and the CaF_2 window with patterned ZnO layer to obtain ~96% reflectivity at around 5 μ m wavelength. In this work, a dielectric-coated flat CaF_2 and a dielectric-coated CaF_2 with patterned ZnO (~200-nm thickness) are used in tandem to generate dual cavity modes separated by ~30 cm⁻¹ at 5 μ m. The frequency separation between the two cavity modes can be tuned by controlling the thickness of the ZnO layer.

Sample Preparation

The W(CO)₆ (Sigma-Aldrich)/coupled-cavity system is prepared in an IR spectral cell (Harrick) containing one flat dielectric CaF₂ mirror and one checkerboard-patterned dielectric CaF₂ mirror, separated by a 12.5 μ m Teflon spacer and filled with W(CO)₆/hexane solution with various concentrations (40 Mm, saturated concentration, 32 mM and 26 mM). The regular W(CO)₆/cavity system is prepared in the same way in an IR spectral cell with two flat dielectric CaF₂ mirrors. The cavity mode finesse is around 14 with $\lambda_{FSR}/\Delta\lambda c$, where λ_{FSR} is the free spectral range and $\Delta\lambda c$ is the FWHM of the resonance.

2D IR spectroscopy

Two-dimensional infrared (2D IR) spectroscopy(21) is applied to investigate the light-matter interaction of a W(CO)₆/microcavity system (detailed 2D IR set up, and data acquisition is described in S1.2). Briefly, a pump-probe geometry is adopted where three IR pulses (Fig. 1a) interact with sample systems. The first IR pump pulse and probe pulse generate two coherent states in the system in t_1 and t_3 , respectively, which will later be Fourier transformed to the frequency domain as ω_1 (pump frequency) and ω_3 (probe frequency). The second IR pump pulse puts the system in a population state during t_2 . All 2D IR spectra in this work are taken at t_2 = 20 ps to avoid interference between pump and probe pulses.

Simulating Nonlinear Spectra

Two linear spectra are simulated, one with all population on the ground vibrational states, corresponding to probe spectra with no IR pump, and another with the ground state population lifted to the excited vibrational states, simulating the probe spectra after IR excitation. The differences between the two spectra are taken to simulate pump-probe spectra.

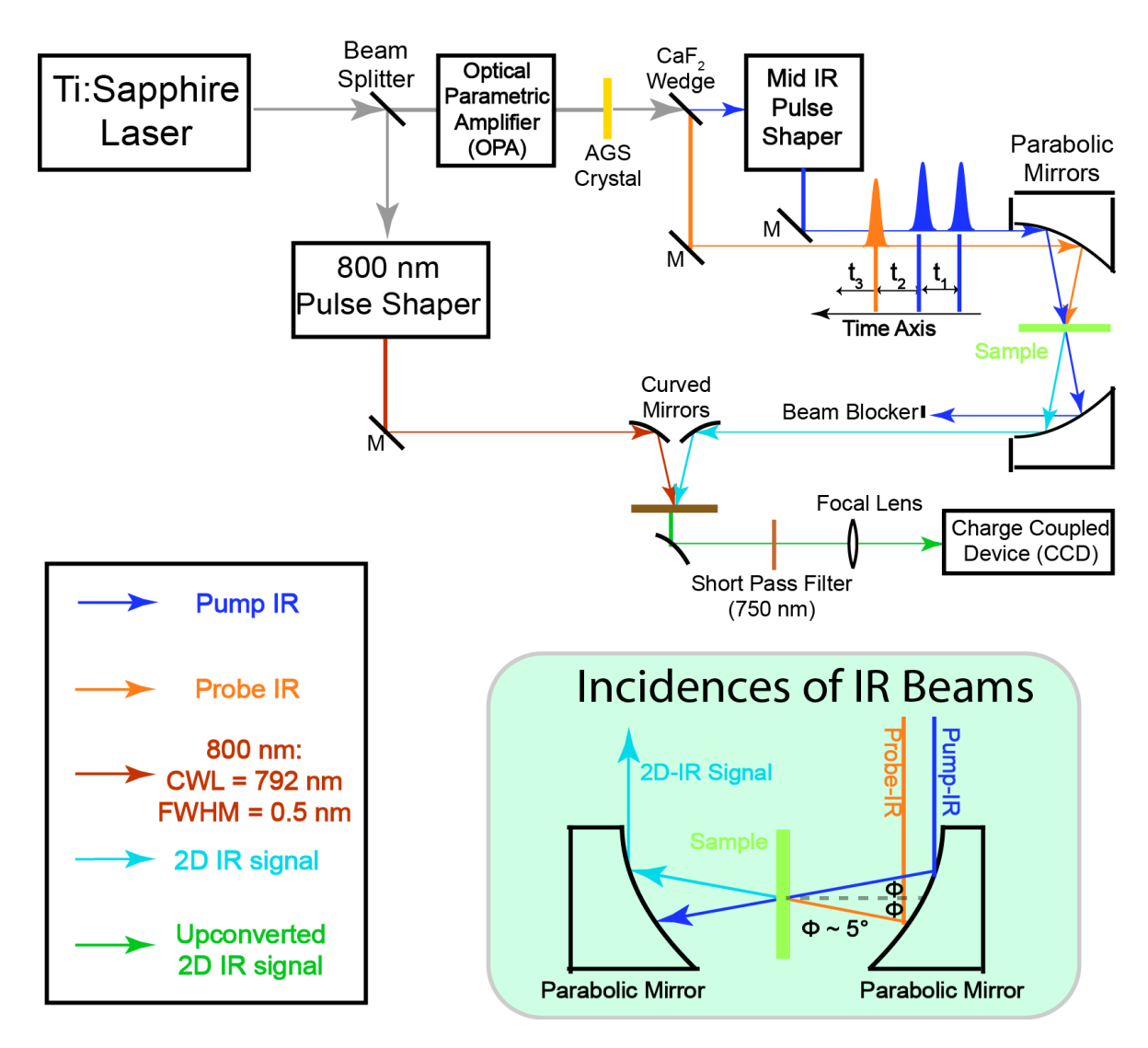


Figure S1. Scheme of two-dimensional infrared experimental setup, where the inset shows the incidence of pump and probe IR beams.

Two-dimensional infrared (2D IR) spectroscopy(2I) is applied to investigate the light-matter interaction of a W(CO)₆/microcavity system. The setup scheme is shown in Fig. S1. 800-nm laser pulses (~35 fs, ~5 W, 1 kHz) generated by an ultrafast Ti:Sapphire regenerative amplifier (Astrella, Coherent) are sent into an optical parametric amplifier (OPA) (TOPAS, LightConversion) which outputs tunable near-IR pulses. The near-IR pulses are converted to mid-IR pulses through a difference frequency generation (DFG) process by a type II AgGaS₂ crystal (Eksma). After DFG, a CaF₂ wedge splits the mid-IR pulse into two parts: the 95% transmitted part is sent into a Ge-Acoustic Optical Modulator based mid-IR pulse shaper (QuickShape, PhaseTech) and is shaped to double pulses, which forms the pump beam arm; the 5% reflected is the probe beam. Both pump (~ 1.1 μ J) and probe (~ 0.2 μ J) are focused by a parabolic mirror (f = 10 cm) and overlap spatially at the sample. The output signal is collimated by another parabolic mirror (f = 10 cm) at a symmetric position and is upconverted to an 800-nm beam at a 5%Mg: LiNbO₃ crystal. The 800-nm beam

out of the OPA passes is spectrally narrowed by a pulse shaper (center wavelength of 791 nm and an FWHM of 0.5 nm or 9.5 cm⁻¹).

The pulse sequence is shown in Fig. S1. Two pump pulses and a probe pulse (pulse duration of $100\sim150$ fs) interact with samples at delayed times (t_1 , t_2 , and t_3). After the first IR pulse, a vibrational coherence is generated, which is converted into a subsequent population state by the second IR pulse and is characterized by scanning t_1 (0 to 6000 fs with 20 fs steps) using the mid-IR pulse shaper. A rotating frame at $t_0 = 1583$ cm⁻¹ is applied to shift the oscillation period to 80 fs and to make the scanning step meet the Nyquist frequency requirement. After waiting for t_2 , the third IR pulse (probe) impinges on the sample, and the resulting macroscopic polarization emits an IR signal. This IR signal is upconverted by a narrow-band 800 nm beam. The upconversion process covers the t_3 time delay, and the 800-nm pulse duration (full width at half maximum = 0.5 nm) determines the scanning length of t_3 . The monochromator and CCD (Andor) experimentally Fourier transform the upconverted signal, thus generating a spectrum along the ω_3 axis. Numerical Fourier transform of the signal along the t_1 axis is required to obtain the spectrum along ω_1 . The resulting 2D IR spectra are plotted against ω_1 and ω_3 . The t_2 time delay is scanned by a computerized delay stage, which is controlled by LabVIEW programs to characterize the dynamic features of the system. A rotational stage is mounted on the sample stage to choose the tilt angle and, therefore, the in-plain wavevector of the driven polaritons.

S2 Theory

S2.1 Model for Transmission of a Single Fabry-Pérot Cavity --- Model 1.

The equation for the transmission of a Fabry-Pérot cavity, based on the transfer matrix model, is listed as equation S1. This expression can provide a basis for relating transient spectra to excited and ground state populations(18).

$$T_{cav}(\bar{\nu}) = \frac{T^2 e^{-\alpha L}}{1 + R^2 e^{-2\alpha L} - 2R e^{-\alpha L} \cos(4\pi n_r L \bar{\nu} + 2\Delta \varphi)}$$
(S1)

This relationship is based on the frequency-dependent absorption coefficient (α) and refractive index (n_r) of the material within the cavity. T, R, L, and $\Delta \varphi$ is the transmission, reflectivity, thickness, and phase shift of the cavity, respectively. We obtain α and n_r by modeling the dielectric function of the cavity load as a sum of Lorentzian oscillators. The real and imaginary components of the dielectric function, ε_1 and ε_2 , are defined as a sum of Lorentzian oscillators i according to

$$\varepsilon_1 = n_{bg}^2 + \sum_i \frac{A_i(\nu_{0i}^2 - \nu^2)}{(\nu_{0i}^2 - \nu^2)^2 + (\Gamma_i \nu)^2} , \qquad (S2)$$

$$\varepsilon_2 = \sum_i \frac{A_i \Gamma_i \nu}{(\nu_{0i}^2 - \nu^2)^2 + (\Gamma_i \nu)^2}$$
 (S3)

where n_{bg} is the background refractive index, A_i the amplitude, v_{0i} the resonant frequency, and Γ_i the full linewidth associated with the i^{th} oscillator. The frequency-dependent refractive index, n_r , and absorption coefficient, α , can be formulated as

$$n_r = \sqrt{\frac{\varepsilon_1 + \sqrt{\varepsilon_1^2 + \varepsilon_2^2}}{2}},$$
(S4)

$$\alpha = 4\pi\nu k = 4\pi\nu \sqrt{\frac{-\varepsilon_1 + \sqrt{\varepsilon_1^2 + \varepsilon_2^2}}{2}}.$$
 (S5)

Initial values of A_i , v_{0i} , and Γ_i are chosen based on the optical response of witness samples, *i.e.*, absorbance for the concentration and pathlengths used.

S2.2 Model for the Transmission of Dual Cavity --- Model 2

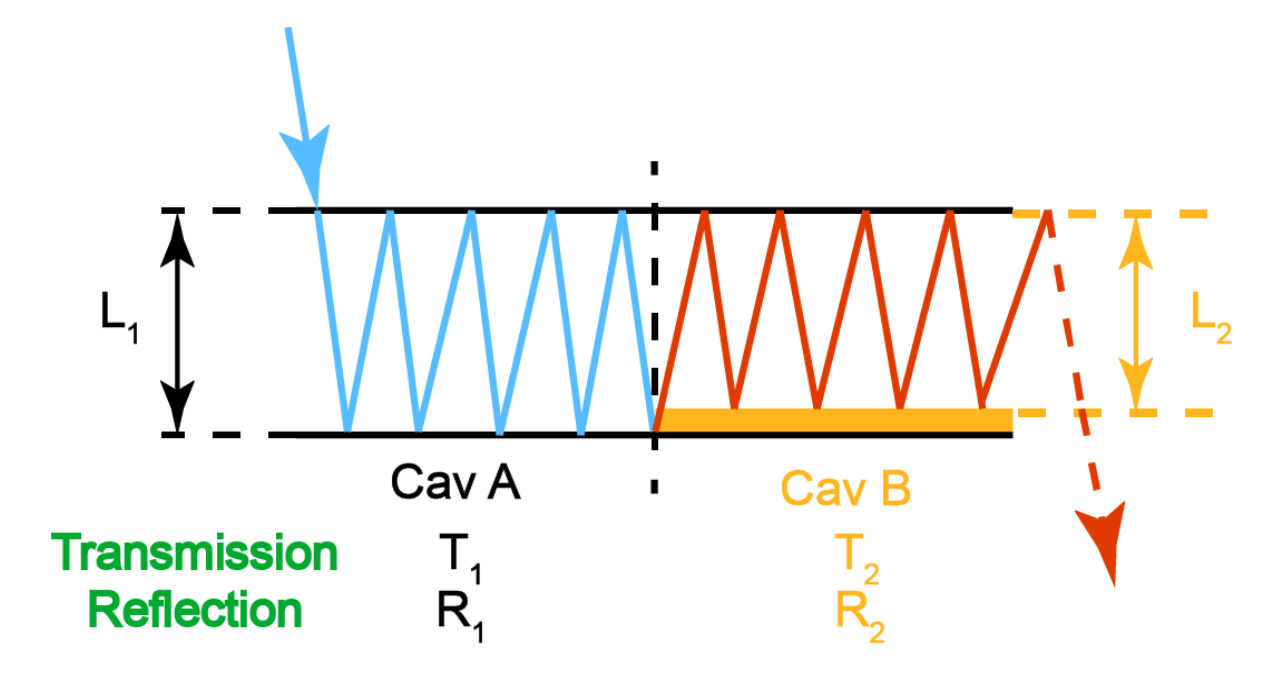


Figure S2. Schematic illustration of intercavity hopping, where the key parameters of simulation for both cavities are labeled.

Model 2, which involves the intercavity photon hopping, can be derived from the model of FP interferometer. The sum of all the transmitted signals can be expressed as

$$I_{Trans} = \left(\frac{E_2}{E_0}\right)^2. \tag{S6}$$

 E_2 is the electric field of all transmitted light, which contains the contribution from pure transmission within cavity A area (with only blue paths) and 'hopped' transmission from cavity A to cavity B (with both blue and red paths). More specifically, $E_2(Cav A)$ is the electric field of incident light from cavity A area reflected a few times and transmit within A-area; while $E_2(Cav A + B)$ is the electric field of incident light entering from cavity A and exiting in B-area. The two contributions are given

$$\begin{split} E_{2}(Cav\,A) &= E_{0}\left(t_{1}t_{1}e^{-\kappa L_{1}} + t_{1}t_{1}r_{1}^{2}e^{-3\kappa L_{1}}e^{i\Delta\phi_{1}} + t_{1}t_{1}r_{1}^{4}e^{-5\kappa L_{1}}e^{2i\Delta\phi_{1}} + \cdots \right. \\ &+ t_{1}t_{1}r_{1}^{2(n-1)}e^{-(2n-1)\kappa L_{1}}e^{(n-1)i\Delta\phi_{1}}\right) \\ &= \left[E_{0}t_{1}t_{1}e^{-\kappa L_{1}}(1+\beta+\beta^{2}+\beta^{3}+\cdots)\right] \\ &- \left[E_{0}t_{1}t_{1}r_{1}^{2n}e^{-(2n+1)\kappa L_{1}}e^{ni\Delta\phi_{1}}(1+\beta+\beta^{2}+\beta^{3}+\cdots)\right] \end{split} \tag{S7}$$

where

$$\boldsymbol{\beta} = r_1^2 e^{-2\kappa L_1} e^{i\Delta\phi_1} \tag{S8}$$

$$(1 + \beta + \beta^2 + \beta^3 + \cdots) = \frac{1}{1-\beta}.$$
 (S9)

$$E_2(Cav A) = \frac{E_0 t_1 t_1 e^{-\kappa L_1}}{1 - r_1^2 e^{-2\kappa L_1} e^{i\Delta\phi_1}} (1 - r_1^{2n} e^{-2n\kappa L_1} e^{ni\Delta\phi_1}).$$
 (S10)

$$\begin{split} E_{2}(Cav \, A + B) &= E_{0} \left(t_{1} t_{2} r_{1}^{2(n-1)} r_{2}^{2} e^{-(2n-1)\kappa L_{1}} e^{(n-1)i\Delta\phi_{1}} e^{-2\kappa L_{2}} e^{i\Delta\phi_{2}} \right. \\ &+ t_{1} t_{2} r_{1}^{2(n-1)} r_{2}^{4} e^{-(2n-1)\kappa L_{1}} e^{(n-1)i\Delta\phi_{1}} e^{-4\kappa L_{2}} e^{2i\Delta\phi_{2}} + \cdots \\ &+ t_{1} t_{2} r_{1}^{2(n-1)} r_{2}^{2m} e^{-(2n-1)\kappa L_{1}} e^{(n-1)i\Delta\phi_{1}} e^{-2m\kappa L_{2}} e^{mi\Delta\phi_{2}} \\ &+ \cdots \quad (till \, m \to \infty) \\ &= \left(E_{0} t_{1} t_{2} r_{1}^{2(n-1)} r_{2}^{2} e^{-(2n-1)\kappa L_{1}} e^{(n-1)i\Delta\phi_{1}} e^{-2\kappa L_{2}} e^{i\Delta\phi_{2}} \right) (1 + \gamma + \gamma^{2} \\ &+ \gamma^{3} + \cdots) \end{split}$$

where

$$\gamma = r_2^2 e^{-2\kappa L_2} e^{i\Delta\phi_2}.$$
 (S12)

$$E_2(Cav A + B) = \frac{E_0 t_1 t_2 r_1^{2(n-1)} r_2^2 e^{-(2n-1)\kappa L_1} e^{(n-1)i\Delta\phi_1} e^{-2\kappa L_2} e^{i\Delta\phi_2}}{1 - r_2^2 e^{-2\kappa L_2} e^{i\Delta\phi_2}}.$$
 (S13)

The sum of all the transmitted signals is given by

$$I_{Trans} = \left(\frac{E_2(Cav A) + E_2(Cav A + B)}{E_0}\right)^2.$$
 (S14)

Plug in

$$T_{i} = t_{i}^{2}, R_{i} = r_{i}^{2}, \alpha = 2\kappa. \tag{S15}$$

 T_i , R_i , L_i and $\Delta \phi_i$ are the transmission, reflection, cavity longitudinal length and phase shift of corresponding cavity area (A: i = 1; B: i = 2), α is the absorptive coefficient of molecules and n represents the number of round trips (in A-area) before photon hopping to the adjacent cavity.

The cavity transmission (model 2) can be expressed as

$$T = \left[\frac{T_1 e^{-\frac{1}{2}\alpha L_1}}{1 - R_1 e^{i\Delta\varphi_1 - \alpha L_1}} \left(1 - R_1^n e^{-n\alpha L_1 + in\Delta\varphi_1} \right) + \frac{\sqrt{T_1 T_2} e^{-\frac{1}{2}\alpha L_1}}{1 - R_2 e^{i\Delta\varphi_2 - \alpha L_2}} \left(R_1^{n-1} e^{-(n-1)\alpha L_1 + i(n-1)\Delta\varphi_1} R_2 e^{-\alpha L_2 + i\Delta\varphi_2} \right) \right]^2$$
(S16)

S2.3 Pump-Probe Fitting Model Based on Model 2.

Based on equation (S16) in S2.2, pump-on (T_{on}) and pump-off (T_{off}) transmission spectra were simulated separately. By subtracting pump-off from pump-on transmission spectra, pump-probe traces (T_{pp}) were obtained. T has the contributions of cavity path A and B, which is related to the amplitude, A_i in equation (S18) below.

For T_{on} and T_{off} , the major change is the value of the absorption coefficient, α . $\alpha(\nu) = 4\pi \frac{\mathbf{k}}{\mathbf{k}}(\nu)\nu$, where $\frac{\mathbf{k}}{\mathbf{k}}(\nu)$ is the imaginary part of the complex refractive index, and ν is frequency. We use equation S17 to compute $\frac{\mathbf{k}}{\mathbf{k}}(\nu)$ and $\alpha(\nu)$, which we use to calculate the transmission based on equation S16.

$$k(v) = \sqrt{\frac{-\varepsilon_1 + \sqrt{\varepsilon_1^2 + \varepsilon_2^2}}{2}}$$
 (S17)

where ε_1 and ε_2 are the real and imaginary parts of dielectric constant, expressed as

$$\varepsilon_{1} = \varepsilon_{inf} + \sum_{i=1}^{2} \left[\frac{A_{i}(\nu_{i}^{2} - \nu^{2})}{(\nu_{i}^{2} - \nu^{2})^{2} + (\Gamma_{i}\nu)^{2}} \right], \quad \varepsilon_{2} = \sum_{i=1}^{2} \left[\frac{A_{i}\Gamma_{i}\nu}{(\nu_{i}^{2} - \nu^{2})^{2} + (\Gamma_{i}\nu)^{2}} \right]$$
(S18)

where we set the background dielectric constant at the infinite frequency to be $\varepsilon_{inf} = 1.77$ (e.g. $\varepsilon_{inf} = n_{bg}^2$, where $n_{bg}=1.33$ for hexane), v_i are the frequencies of the $0 \to 1$ and $1 \to 2$ asymmetric stretch transitions of W(CO)₆ given by $v_1 = 1983$ cm⁻¹, and $v_2 = 1968$ cm⁻¹, and the v_i are the linewidths of the corresponding vibrational modes (v_1 and v_2 are 3.0 and 4.5 cm⁻¹, respectively).

The amplitude A_i at corresponding states (A_1,A_2 , and A_3 for ground, first excited, and second excited states, respectively) represents the relative population at these states and are affected by IR pumping. For pumpon spectra, $A_1 = \mathcal{A}$ -dc1-dc12 (path A) or \mathcal{A} -dc2-dc22 (path B), $A_2 = dc1$ (path A) or dc2 (path B) and $A_3 = dc12$ (path A) or dc22 (path B), where \mathcal{A} is the overall concentration of the vibrational modes, dc1 and dc12

are the relative population to the first and second excited states in cavity A, respectively, and da2 and dc22 are the corresponding populations in cavity B. For pump-off spectra, $A_1 = \mathcal{R}$ (both path A and B), $A_2 = A_3 = 0$ (both path A and B). The number of round trips (n) in the starting cavity are labeled as N_1 and N_2 , for cavity path A and B, respectively. We found $N_1=7$ and $N_2=10$, which best reproduce the experimental linear spectra. Considering the cavity finesse is around 14, which represent the round trips of the cavity photon, the N_1 and N_2 suggest that photon hopping happens in both cavity A and B. The physical meanings of all the fitting parameters are summarized below. Their values are listed in S3.2.

Physical Meanings of Fitting Parameters:

L₁: the thickness of cavity A

L₂: the thickness of cavity B

T₁: transmission of cavity mirror for cavity A

T₂: transmission of cavity mirror for cavity B

N₁: number of round trips in cavity A of path cavity A

N₂: number of round trips in cavity B of path cavity B

A: Amplitude of molecular transitions, related to static concentration of molecules

dc1: Amplitude of optical transitions of 1st excited states in cavity A

dc12: Amplitude of optical transitions of 2nd excited states in cavity A

dc2: Amplitude of optical transitions of 1st excited states in cavity B

dc22: Amplitude of optical transitions of 2nd excited states in cavity B

S3 Supplementary Data

S3.1 Transient Pump-Probe and 2D IR Spectra of Molecular Vibrational Polariton Systems.

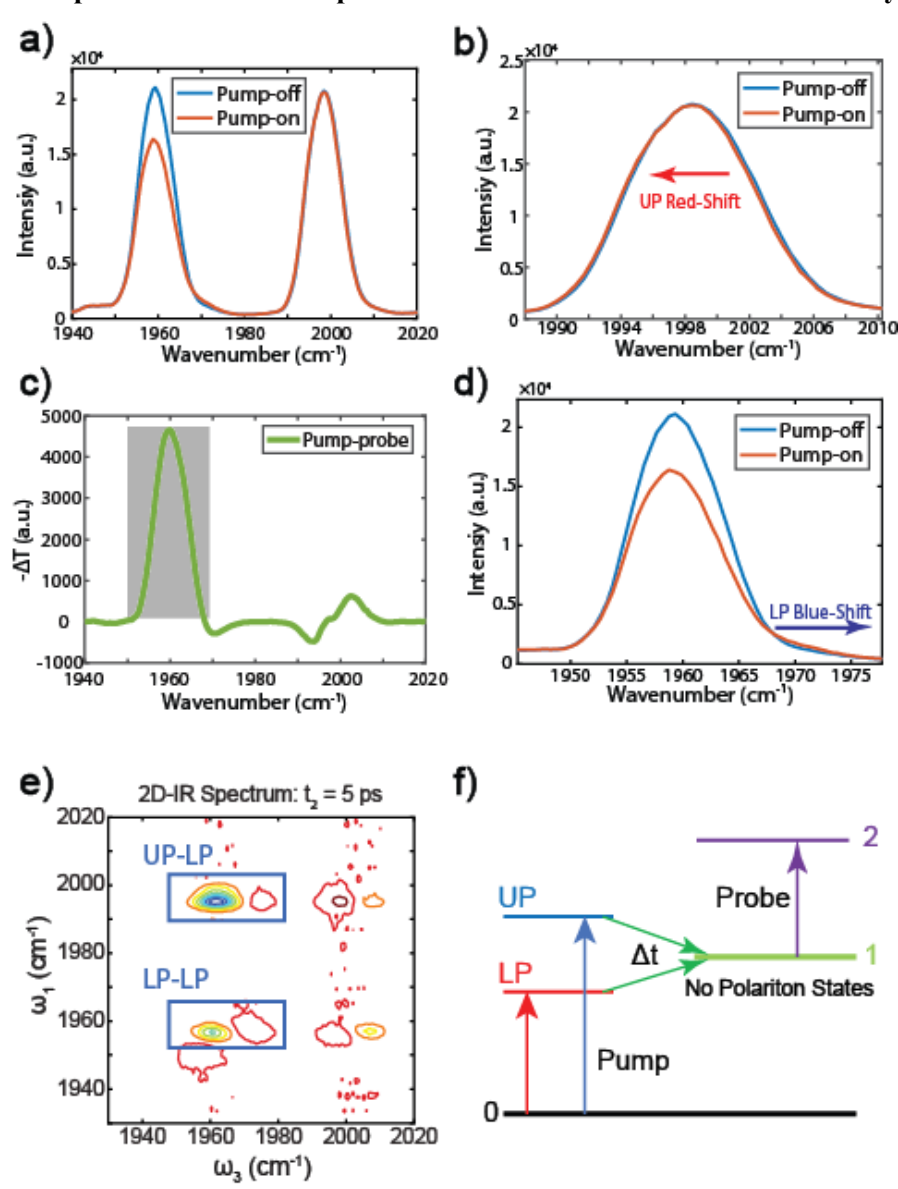


Figure S3. Pump probe, 2D IR spectra of molecular polaritons. a) Pump-on and pump-off spectra of strongly coupled W(CO)6/hexane system in transient pump-probe experiment at t2 = 25 ps; b) UP branch zoom-in; c) pump-probe spectrum at t2 = 25 ps; d) LP branch zoom-in; (e) 2D IR spectrum of strongly coupled W(CO)6/hexane system at t2 = 5 ps; (f) Schematic illustration of the population transfer process when the polariton system is in equilibrium (t2 > 3 ps).

Fig. S3 shows representative transient pump-probe spectra(4, 6, 19) under strong coupling conditions (1 Vibrational mode + 1 Cavity mode), along with 1D transmission polariton spectra (strongly coupled W(CO)₆ in hexane) under pump-on and pump-off conditions, at $t_2 > 3$ ps (Fig. S3a). When the pump is

turned on, the UP resonance undergoes a shift towards a lower frequency (Fig. S3b). Under the same condition, the LP lineshape acquires a small positive shoulder appears at a higher frequency, which corresponds to a blue shift (Fig. S3d). These shifts are small but consistent and result in a derivative lineshape in the transient pump-probe spectrum (Fig. S3c). The peak-shift is induced by the Rabi splitting contraction, which arises due to the pump-induced reduction of the molecular ground-state population. The substantially reduced LP transmission upon pumping, and consequently the absorptive lineshape in the pump-probe spectra, results from that the dark mode overtone v_{12} transition (from first excited to second excited states, purple arrow in Fig. S3f) is near-resonant with LP transition. As a result, v_{12} becomes visible through the LP transmission window. Thus, when LP and v_{12} are near resonance, the appearance of a strong absorptive transient signal at ω_{LP} is a signature of populating the first excited state of dark modes.

While pump-probe spectroscopy allows us to follow polariton to dark state dynamics, the state-selective 2D IR spectrum (Fig. S3e) can disentangle the dynamics: The UP-LP peak labeled in Fig. S3e (left-top) represents the population transfer from UP state to dark mode while the LP-LP peak (Fig. S3e, left-bottom) is mainly due to the LP to dark mode population transfer. As summarized in Fig. S3f, it is believed that the UP/LP population transfer to dark modes in a fast timescale, which subsequently makes the dark mode v_{12} appear in the pump-probe or 2D spectra. We can learn the polariton dynamics by measuring dynamics of LP peak in pump-probe spectra (integrating over the transient pump-probe peak near LP position, e.g., shaded area in Fig.S3c)), and dynamics of UP-LP and LP-LP peaks from 2D IR spectra (integrating 2D spectral peaks at UP-LP and LP-LP area, e.g., green boxes in Fig. S3e).

S3.2 Simulation of the Rest Spectral Cuts of 2D IR of 40-mM W(CO)₆ in Hexane

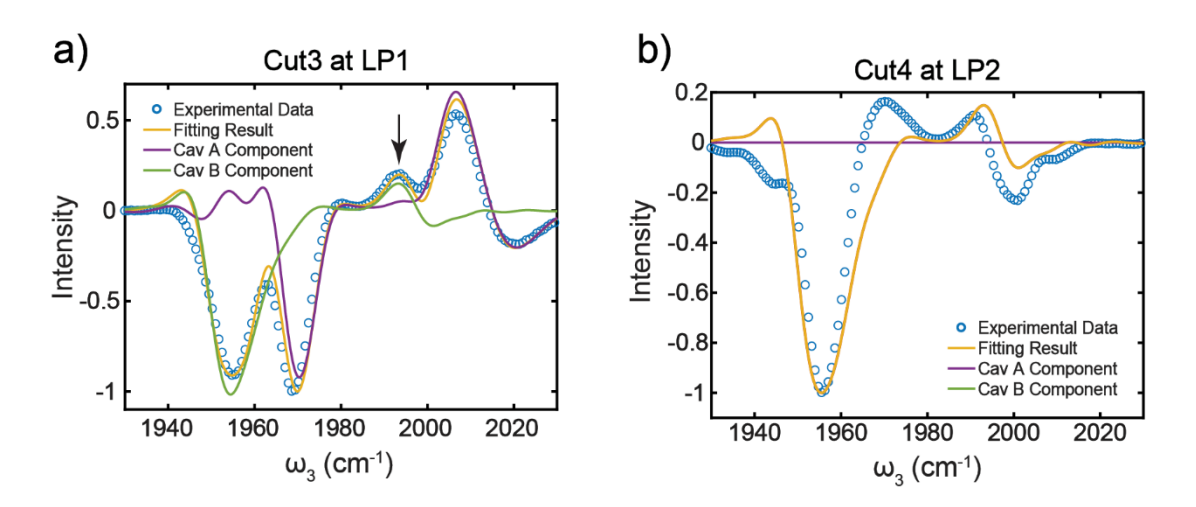


Figure S4. a) 2D IR spectral cut at $\omega_I = \omega_{LP1}$ and b) at $\omega_I = \omega_{LP2}$, with simulation results of the contributions from pure cavity A component (purple trace), pure cavity B component (green trace) and cavity A + B components (yellow trace).

Fig. S4a and b show the experimental data and simulation results of LP1 and LP2 spectral cuts. The interpretation of the LP1 spectral cut at 40 mM is similar to the one of the UP1 spectral cut in the main manuscript when describing Fig. 2c, while the results of LP2 spectral cuts show similar features as UP2 cut in Fig. 2d. When LP1 from cavity A is pumped, UP2 from cavity B is perturbed, which results in LP1-UP2 cross-peak (labeled by an arrow in Fig. S4a). The dark mode excited state in cavity B also contributes to the large peak at 1955 cm⁻¹. In contrast, the LP2 cut shows no cross-peak around the LP2-UP1 area.

The fitting parameters of all four spectral cuts (cut 1 at UP1, cut 2 at UP2, cut 3 at LP1 and cut 4 at LP2) are shown in the following table.

Table S1. Fitting parameters in model 2 for dual-cavity 2D IR spectral cuts at 40 mM.

| | $\mathcal{A}(\mathrm{cm}^{-1})$ | dc1(cm ⁻¹) | dc12(cm ⁻¹) | dc2(cm ⁻¹) | dc22(cm ⁻¹) |
|--|---------------------------------|------------------------|-------------------------|------------------------|-------------------------|
| Cut 1 at UP1 (2010 cm ⁻¹) | 2600 | 1100 | 10 | 320 | 30 |
| Cut 2 at UP2 (1995 cm ⁻¹) | 2600 | 0 | 0 | 500 | 70 |
| Cut 3 at LP1 (1970 cm ⁻¹) | 2600 | 1100 | 10 | 350 | 60 |
| Cut 4 at LP2 | 2600 | 0 | 0 | 500 | 60 |

(1955 cm⁻¹)

We also used common parameters to describe the coupled cavities for all of the 2D IR spectral cuts, at any molecular concentrations in this and the following sections: L_1 =0. $\frac{001250}{001250}$ cm; L_2 =0. $\frac{001269}{001269}$ cm; T_1 =0.109; T_2 =0.105; N_1 =7; N_2 =10.

S3.3 2D IR Spectral Features and Their Simulation Results of Polariton Systems with Other Concentrations

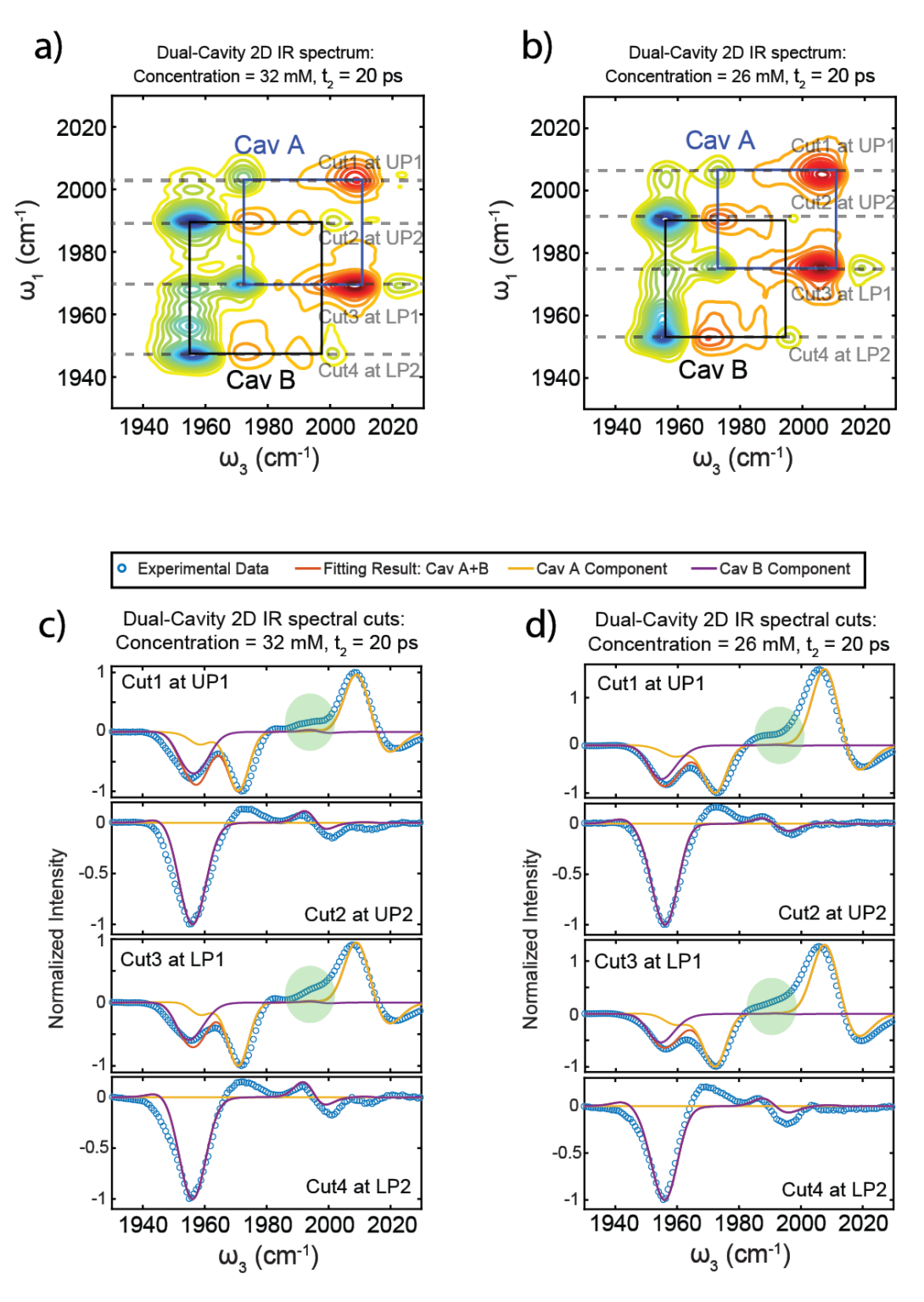


Figure S5. 2D IR spectra of $W(CO)_6$ /hexane in dual-cavity at $t_2 = 20$ ps with molecular concentrations of (a) 32 mM, (b) 26 mM; 2D IR spectral cuts at four polaritonic states labeled in a and b with molecular concentrations of (c) 32 mM, and (d) 26 mM. All data were collected at beam incidence angle at 11.3 °

The 2D IR feature of dual-cavity strongly coupled systems with lower concentrations shows smaller cross-peak intensities (shaded green areas in Fig. S5c and d) compared to the ones in Fig. 2b. The fitting results confirmed that although both cavity A and B have contributions to the signal, the cavity B component is relatively smaller compared to the one in Fig. 2c with a molecular concentration of 40 mM. The concentration variation experiments provide a convenient way to control the intercavity coupling strength macroscopically.

Table S2. Fitting parameters in model 2 for dual-cavity 2D IR spectral cuts at 32 mM.

| | $\mathcal{A}(\mathrm{cm}^{-1})$ | dc1(cm ⁻¹) | dc12(cm ⁻¹) | dc2(cm ⁻¹) | dc22(cm ⁻¹) |
|---------------------------------------|---------------------------------|------------------------|-------------------------|------------------------|-------------------------|
| Cut 1 at UP1 (2010 cm ⁻¹) | 2450 | 450 | 5 | 30 | 3 |
| Cut 2 at UP2 | 2450 | 0 | 0 | 1200 | 50 |
| (1995 cm ⁻¹) | | | | | |
| Cut 3 at LP1 (1970 cm ⁻¹) | 2450 | 450 | 0 | 17 | 3 |
| Cut 4 at LP2 | 2470 | 0 | | 4 = 0 0 | 100 |
| (1955 cm ⁻¹) | 2450 | 0 | 0 | 1500 | 180 |

Table S3. Fitting parameters in model 2 for dual-cavity 2D IR spectral cuts at 26 mM.

| | A (cm ⁻¹) | dc1(cm ⁻¹) | dc12(cm ⁻¹) | dc2(cm ⁻¹) | dc22(cm ⁻¹) |
|--|------------------------------|------------------------|-------------------------|------------------------|-------------------------|
| Cut 1 at UP1 (2010 cm ⁻¹) | 2050 | 550 | 5 | 16 | 4 |
| Cut 2 at UP2 (1995 cm ⁻¹) | 2050 | 0 | 0 | 1500 | 100 |
| Cut 3 at LP1 (1970 cm ⁻¹) | 2050 | 450 | 0 | 10 | 3 |
| Cut 4 at LP2 (1955 cm ⁻¹) | 2050 | 0 | 0 | 1700 | 700 |

S3.4 Four-by-Four Matrix Models the Intercavity Coupling along with Coupling between Cavity Modes and Molecular Vibrational Modes

In our dual-cavity system, one vibrational mode would strongly couple to the two cavity modes. One would first expect the hybridization forms three new polariton states which are the three eigenstates derived from the matrix below.

$$\begin{vmatrix} CavA & g_c & G \\ g_c & CavB & G \\ G & G & Vib \end{vmatrix}$$
 (S19)

Where g_c is the coupling between the two cavities and the G is the molecule-cavity coupling strength. However, this contradicts with our experimental results shown in the transmission spectrum (Fig. 1e) where four new polariton peaks show up vis strong coupling in this system. Therefore, we can conclude that the vibrational mode would strongly couple to cavity A and B separately.

To test whether intermolecular coupling plays a role in the observed spectra, we constructed the Hamiltonian in S20, and let Cav A/Cav B, G (strong coupling strength), and g_m (intermolecular coupling strength between vib A and vib B modes) to optimize and simulate the spectral position of our experimental data. The experimental peak positions of LP2, LP1, UP2 and UP1 are 1956, 1969, 1998 and 2013 cm⁻¹ and the vib A and vib B energies are set to be 1983 cm⁻¹. We found after optimization (the best matching between the diagonalized frequency of S20 and experimental peak positions), g_m=0, which indicates that the direct intermolecular interaction is negligible. Therefore, we note the intermolecular interaction are negligible to the linear IR.

$$\begin{pmatrix}
Vib A & g_m & G & 0 \\
g_m & Vib B & 0 & G \\
G & 0 & Cav A & 0 \\
0 & G & 0 & Cav B
\end{pmatrix}$$
(S20)

To better quantitatively understand the coupling between cavity modes and between vibrational modes and cavity modes, we further generated the following four-by-four matrix (25).

$$\begin{pmatrix} Vib \ A & 0 & G & g \\ 0 & Vib \ B & g & G \\ G & g & Cav \ A & g_c \\ g & G & g_c & Cav \ B \end{pmatrix} \begin{pmatrix} \alpha_{VibA} \\ \alpha_{VibB} \\ \alpha_{CavA} \\ \alpha_{CavB} \end{pmatrix} = E \begin{pmatrix} \alpha_{VibA} \\ \alpha_{VibB} \\ \alpha_{CavA} \\ \alpha_{CavB} \end{pmatrix}$$
(S21)

In the matrix, (Cav A) and (Cav B) terms are the energies of both cavity modes, and (Vib A) and (Vib B) represent the energy of corresponding vibrational mode in each cavity. In this model, strong coupling would occur between (Cav A) and (Vib A) or (Cav B) and (Vib B) with coupling strength, G. Between (Cav A) and (Vib B) or (Cav B) and (Vib A), on the other hand, weak coupling happens with strength, g. G and g should be proportional to the square root of molecular concentration theoretically, so we made g = G/R and used the new parameter, R (ratio between G and g), to correlate G with g.

We optimized the coupling constants and the cavity resonance by using the matrix model to fit the polariton resonance peak positions at different concentrations (G, g, g_c, (Cav A) and (Cav B) (Vib A and Vib B are set to 1983 cm⁻¹, representing the vibrational frequency of W(CO)₆ in hexane, summarized in Table S4). We then used the optimized fitting parameters to solve the eigenvalues and Hopfield coefficients ($|\alpha_{VibA}|^2$, $|\alpha_{VibB}|^2$, $|\alpha_{CavA}|^2$, and $|\alpha_{CavB}|^2$). The table below summarizes the results.

Table S4. Fitting parameters of the four-by-four matrix compared to experimental data.

| Unit: cm ⁻¹ | Cav A = 1997; Cav B = 1973; $g_c = 1.1$; $g=G/R$ (R=5.8) | | | | | | |
|------------------------|---|---------|----------------|---------|----------------|---------|--|
| Conc. | 40 mM (G 20.6) | | 32 mM (G 19.2) | | 26 mM (G 17.8) | | |
| | Expt | Fitting | Expt | Fitting | Expt | Fitting | |
| LP2 | 1956.0 | 1956.0 | 1957.0 | 1957.0 | 1958.0 | 1957.9 | |
| LP1 | 1969.0 | 1969.0 | 1971.0 | 1971.1 | 1972.0 | 1972.1 | |
| UP2 | 1998.0 | 1998.0 | 1996.0 | 1996.0 | 1994.0 | 1994.3 | |
| UP1 | 2013.0 | 2013.0 | 2013.0 | 2013.0 | 2012.0 | 2011.7 | |

The fitted eigenvalues match with the experimental polaritonic frequencies very well. We further calculated the corresponding Hopfield coefficients for each polaritonic states (eigenstates). As we stated in the manuscript the mixing component, e.g. $|\alpha_{VibB}|^2$ for UP1 and LP1 and $|\alpha_{VibA}|^2$ for UP2 and LP2, are the key to the intercavity coupling.

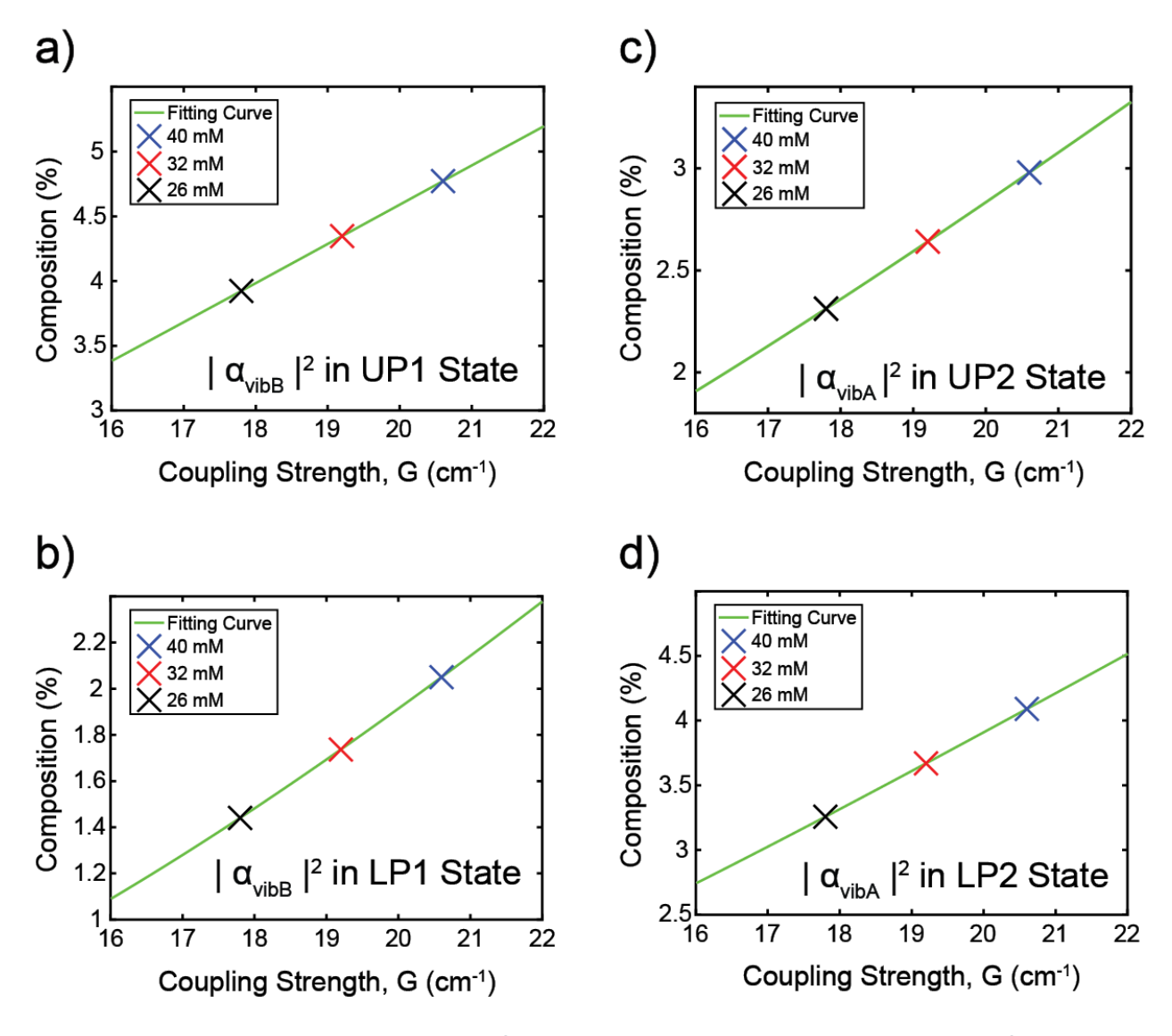


Figure S6. Hopfield coefficient, $|\alpha_{VibB}|^2$ in (a) UP_1 and (c) LP_1 states, and $|\alpha_{VibA}|^2$ in (b) UP_2 and (d) LP_2 states.

Fig. S6 shows that as molecular concentration decreases from 40 mM to 26 mM, G varies from 20.6 cm⁻¹ to 17.8 cm⁻¹, roughly matching the square-root-law to the molecular concentration. $|\alpha_{VibB}|^2$ for UP1 and LP1, as well as $|\alpha_{VibA}|^2$ for UP2 and LP2, are reduced with smaller molecular concentrations. The results of Fig. S6 qualitatively confirmed that as molecular concentration drops, the mixing between cavities decreases, so would the intercavity coupling.

S3.6 2D IR Dynamics

 ω_3 (cm⁻¹)

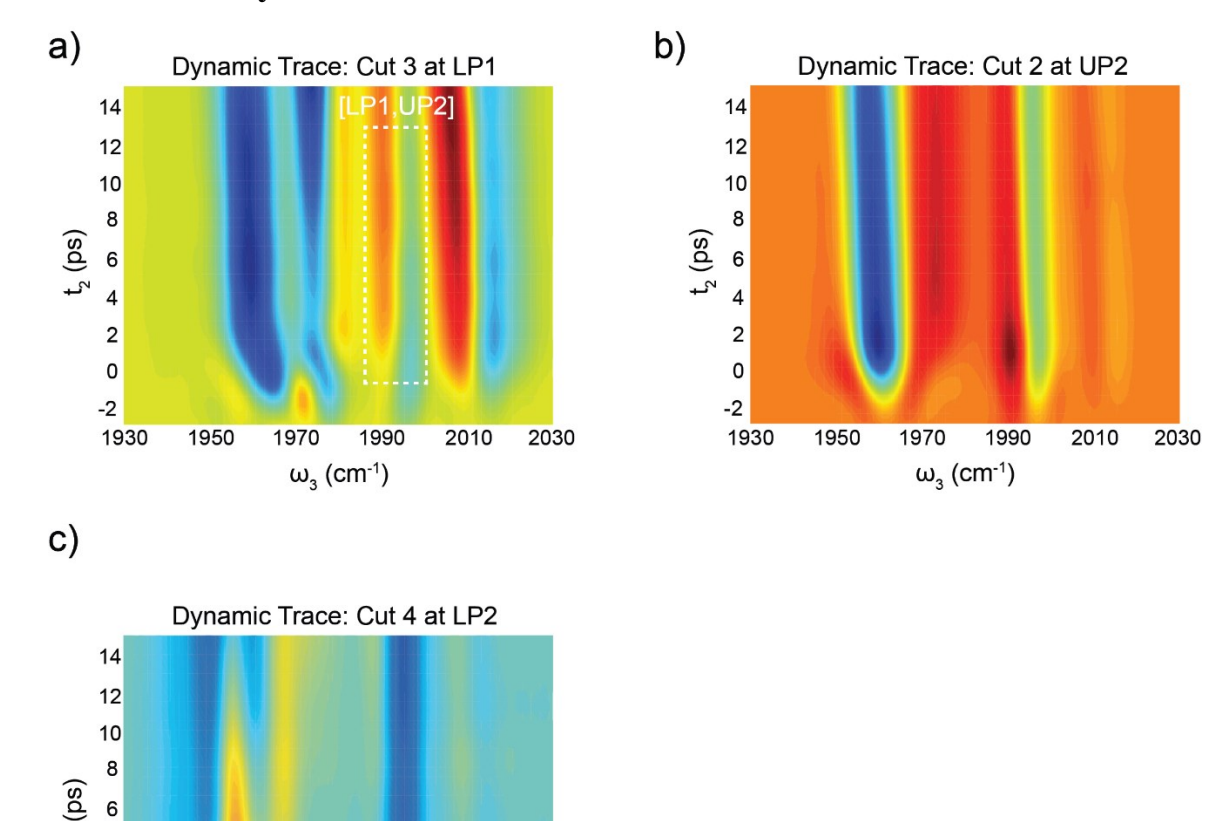


Figure S7. 2D IR dynamics at (a) $\omega_{pump} = \omega_{LP1}$, (b) $\omega_{pump} = \omega_{UP2}$ and (c) $\omega_{pump} = \omega_{LP2}$.

The Fig. S7a show the 2D IR dynamics of the spectral cut at LP1 states. The features in the white dashed boxes are similar to the ones in Fig. 2f (UP1 cut), while for the dynamics at UP2 and LP2 spectral cuts (Fig. S7b and c), most of the features are only from one set of polaritons (LP2/UP2), further confirming the mechanism mentioned in the manuscript.

S3.7 IR Incidence Angle Dependence

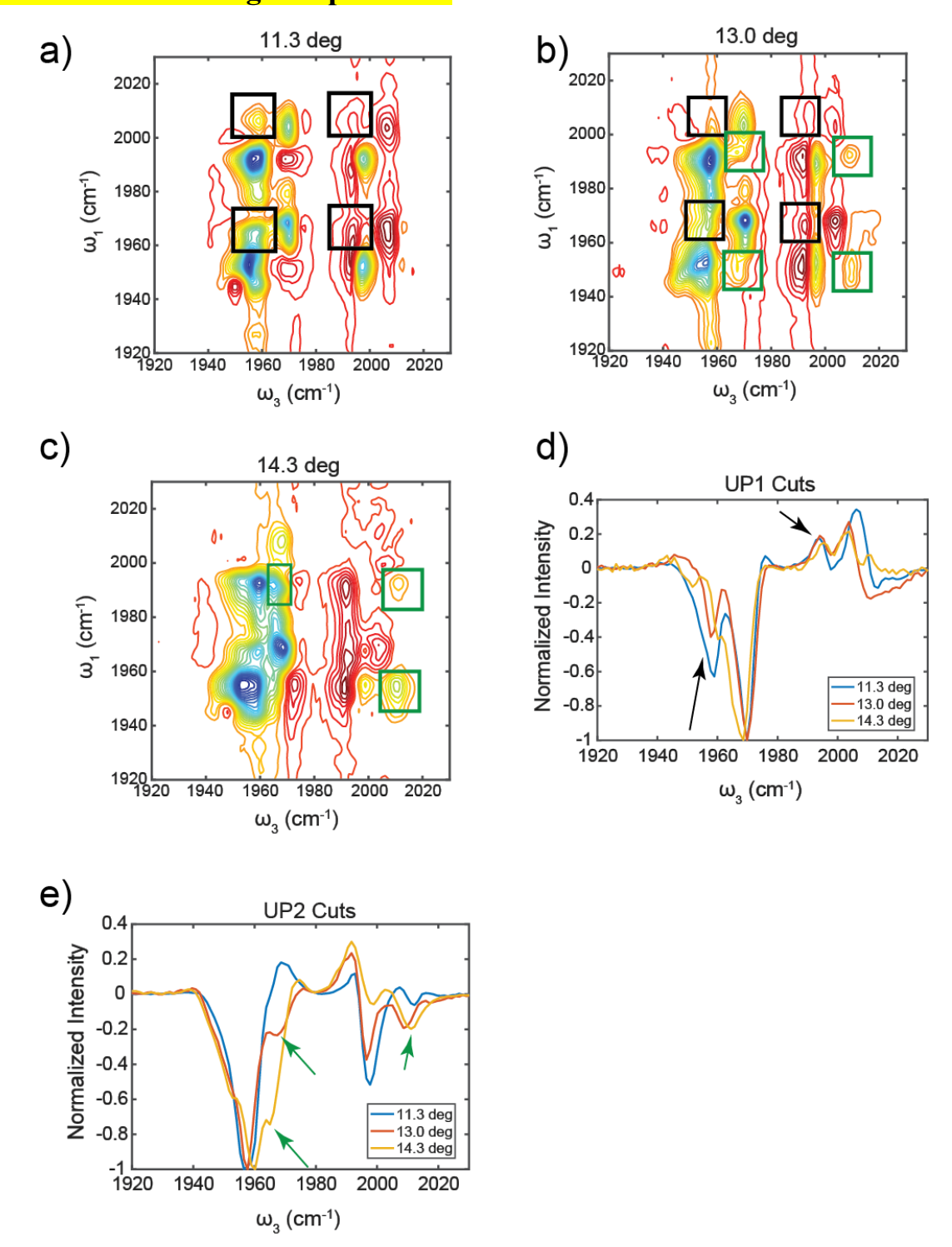


Figure S8. 2D IR spectra of dual-cavity polaritons with IR incidence angles of (a) 11.3 deg, (b) 13.0 deg and (c) 14.3 deg; 2D IR spectral cuts at pump at (de) UP1 state and (e) UP2 state. The intercavity interaction cross peaks due to pumping cavity A (B) are labeled in black (green) boxes

and the black and green arrows serve as eye-guide for intercavity interaction cross peaks of the spectral cuts.

We performed an additional control experiments where the IR incidence angle has been tuned from 11.3 to 14.3 degrees to control the photon hopping pathways. The results shown in Fig. S8 indicate that the intercavity coupling highly depends on the IR incidence angle. Fig. S8a-c show the 2D IR spectra of dual-cavity systems under different IR incidence angles, with spectral cuts shown in Fig. S8d and e, where 11.3-deg and 13.0-deg system shows cross-peak signals upon pumping LP1/UP1 states (black boxes in a-b), while 13.0-deg and 14.3-deg system shows cross-peak signals upon pumping LP2/UP2 states (green boxes in b-c). In summary, the incidence angle would change the possibility of intercavity interaction pathways, which further support that the intercavity interaction could be momentum dependent. The result of this control experiment would be another point to rule out the contribution of the polariton-enhanced intermolecular interactions.

S3.8 Transmission IR Image of Coupled-Cavity Polaritons

The IR imaging of the dual cavity system provides further insights to the checkerboard pattern. We project the IR image of the dual cavity onto the spectrograph slit and image a slice of it along the vertical axis (setup shown in Fig. S9, spatial resolution 10 microns). The slice is then dispersed in the frequency domain along the horizontal axis (Fig. 1j). In the frequency-spatial plot, we can clearly identify two pairs of polaritons displaced from each other vertically. We fitted the vertical distributions of polariton transmission spectrum in cavity A and B into Gaussian functions $(a \cdot \exp\left(-\frac{(x-b)^2}{c^2}\right))$, where a is the amplitude, b is the peak position and c is the width of polariton modes). The peak positions of UP1 and UP2 modes are fitted to be 116 and 69 microns, and the widths of UP1 and UP2 states are 64 and 59 microns. The vertical width of both polariton modes are larger than the lateral width of the cavity in the checkerboard pattern of 50 microns, which suggests that each square pattern supports its own cavity mode, and the mode decays into the neighboring cavities.

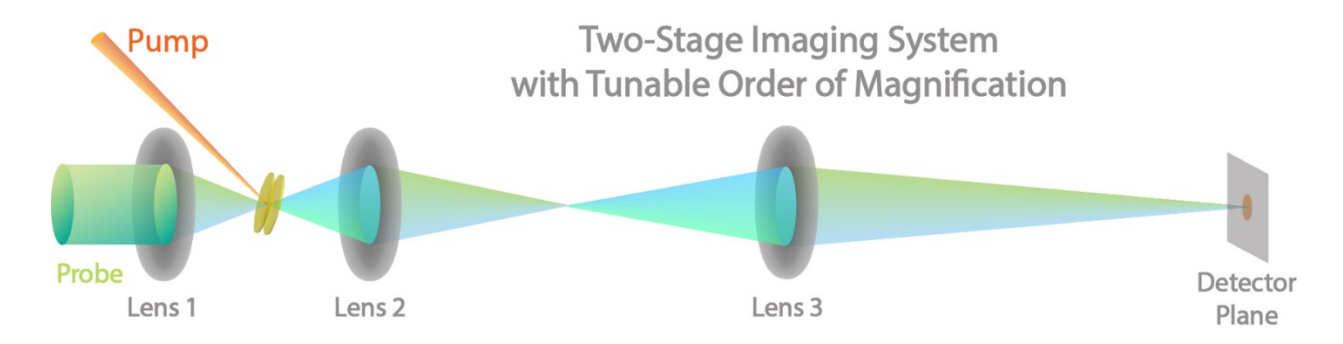


Figure S9. Schematic illustration of 2D IR-imaging setup.

S3.9 2D IR Spectrum of Combination of Detuned Regular Systems

To mimic the nonlinear signals of the dual-cavity system, we have taken two sets of 2D IR spectra of the regular polariton with each of which proper detuned to match one set of the polaritons in the coupled cavity systems. We then add the two 2D IR spectra together (Fig.S10). By comparing Fig. S10 and Fig. 2a in the main text, there are four extra cross-peaks in the green boxes in Fig. 2a which would not be observed experimentally in Fig. S10 systems. These new cross-peaks were unexpected and further support that intercavity polaritonic interaction do exist in the coupled cavity systems.

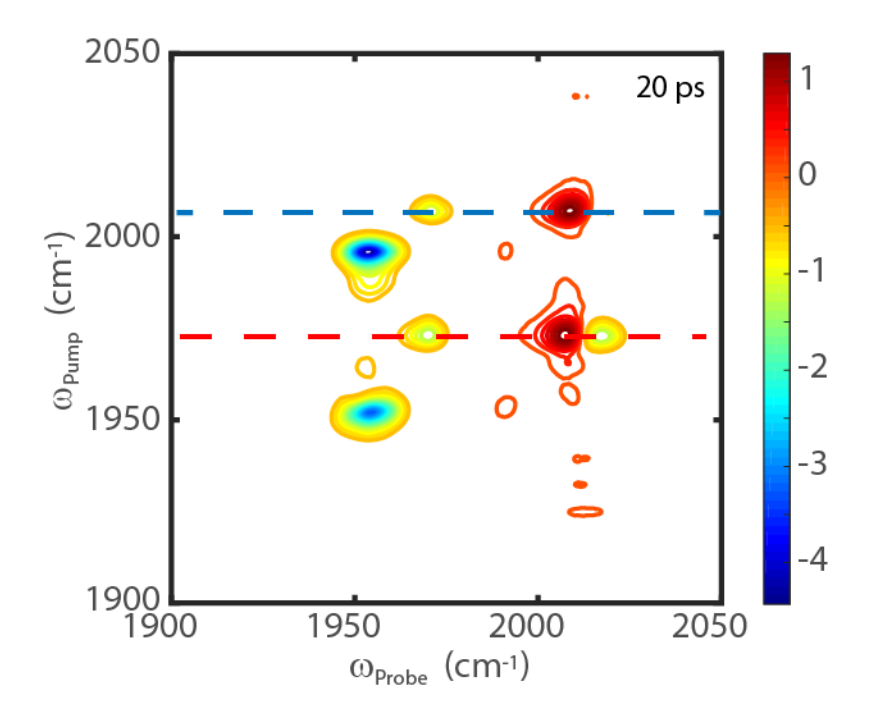


Figure S10. 2D IR spectrum of combination of detuned regular systems to mimic dual-cavity responses without intercavity interactions.